

Magma Reservoir Beneath Azumayama Volcano, NE Japan as Inferred from Three-dimensional Electrical Resistivity Image by Magnetotellurics

Masahiro Ichiki (✉ ichiki@tohoku.ac.jp)

Graduate School of Science, Tohoku University <https://orcid.org/0000-0003-0814-1265>

Toshiki Kaida

Graduate School of Science, Tohoku University

Takashi Nakayama

Graduate School of Science, Tohoku University

Satoshi Miura

Graduate School of Science, Tohoku University

Mare Yamamoto

Graduate School of Science, Tohoku University

Yuichi Morita

Earthquake Research Institute, The University of Tokyo

Makoto Uyeshima

Earthquake Research Institute, The University of Tokyo

Full paper

Keywords: magnetotellurics, electrical resistivity, electrical conductivity, magma reservoir, melt fraction, permeability, percolation threshold, change point, hydrothermal fluid, Mogi source

Posted Date: January 7th, 2021

DOI: <https://doi.org/10.21203/rs.3.rs-139301/v1>

License: © ⓘ This work is licensed under a Creative Commons Attribution 4.0 International License.

[Read Full License](#)

Version of Record: A version of this preprint was published at Earth, Planets and Space on July 27th, 2021. See the published version at <https://doi.org/10.1186/s40623-021-01451-y>.

1 **Title**

2 **Magma reservoir beneath Azumayama Volcano, NE Japan as inferred from three-**
3 **dimensional electrical resistivity image by magnetotellurics**

4 Masahiro Ichiki, Research center for prediction of earthquakes and volcanic eruptions,
5 Graduate School of Science, Tohoku University, 6-6 Aoba, Aramaki, Aoba-ku, Sendai
6 980-8578, Japan, ichiki@tohoku.ac.jp

7 Toshiki Kaida, Research center for prediction of earthquakes and volcanic eruptions,
8 Graduate School of Science, Tohoku University, 6-6 Aoba, Aramaki, Aoba-ku, Sendai
9 980-8578, Japan, toshiki.kaida.a5@tohoku.ac.jp

10 Takashi Nakayama, Research center for prediction of earthquakes and volcanic eruptions,
11 Graduate School of Science, Tohoku University, 6-6 Aoba, Aramaki, Aoba-ku, Sendai
12 980-8578, Japan, takashi.nakayama.c8@tohoku.ac.jp

13 Satoshi Miura, Research center for prediction of earthquakes and volcanic eruptions,
14 Graduate School of Science, Tohoku University, 6-6 Aoba, Aramaki, Aoba-ku, Sendai
15 980-8578, Japan, miura3104@tohoku.ac.jp

16 Mare Yamamoto, Research center for prediction of earthquakes and volcanic eruptions,

17 Graduate School of Science, Tohoku University, 6-6 Aoba, Aramaki, Aoba-ku, Sendai

18 980-8578, Japan, mare@tohoku.ac.jp

19 Yuichi Morira, Earthquake Research Institute, The University of Tokyo, 1-1-1 Yayoi,

20 Bunkyo-ku, Tokyo 113-0032, Japan, morita@eri.u-tokyo.ac.jp

21 Makoto Uyeshima, Earthquake Research Institute, The University of Tokyo, 1-1-1 Yayoi,

22 Bunkyo-ku, Tokyo 113-0032, Japan, uyeshima@eri.u-tokyo.ac.jp

23 **Corresponding author**

24 Masahiro Ichiki, Research center for prediction of earthquakes and volcanic eruptions,

25 Graduate School of Science, Tohoku University, 6-6 Aoba, Aramaki, Aoba-ku, Sendai

26 980-8578, Japan, ichiki@tohoku.ac.jp

27

28 **Abstract**

29 An electrical resistivity image beneath Azumayama Volcano, NE Japan is modeled using
30 magnetotellurics to probe the magma/hydrothermal fluid distribution. The 3-D inversion
31 modeling images the conductive magma reservoir beneath Oana crater at depths of 3–15
32 km. The resolution scale for the conductor is 5 km by checkerboard resolution tests and
33 the 67 % and 90 % confidential intervals of resistivity are 0.2–5 Ωm and 0.02–70 Ωm ,
34 respectively, for the region of less than 3 Ωm resistivity. The shallower part of the
35 conductor is not explained by a water-saturated (5.5 wt %) dacitic melt, and the more
36 probable interpretation is that it consists of a water-saturated, dacitic melt-silicic rock-
37 hydrothermal fluid complex. The deeper part of the conductor is interpreted as a water-
38 saturated (8 wt %) andesitic melt-mafic rock complex. The Mogi inflation source
39 determined from GNSS and tilt data is located near the top boundary of the conductor at
40 a depth of 2.7–3.7 km, which suggests that the ascent of hydrothermal fluids exsolved
41 from the dacitic melt is interrupted by the impermeable wall and conduit. Assuming two
42 phases of hydrothermal fluid and silicic rock, the resistivity at the inflation source,
43 regarded as the upper bound resistivity of the conductor, is realized by the hydrothermal
44 fluid fraction below the percolation threshold porosity in an effusive eruption. This

45 indicates that the percolation threshold porosity in an effusive eruption characterizes the

46 impermeable wall and conduit associated with the Mogi inflation source.

47 **Keywords**

48 magnetotellurics, electrical resistivity, electrical conductivity, magma reservoir, melt

49 fraction, permeability, percolation threshold, change point, hydrothermal fluid, Mogi

50 source

51

52 **Main Text**

53 **1. Introduction**

54 Great earthquakes have often triggered eruptions in neighboring volcanoes
55 (Nishimura, 2017; Koyama, 2015; Bebbington & Marzocchi, 2011). After the 2011
56 Tohoku-Oki Earthquake, the seismicities of deep low-frequency tremor and of volcano-
57 tectonic earthquake have turned active beneath a few volcanoes in northeastern (NE)
58 Japan (e.g. Ikegaya & Yamamoto, 2020; Yamamoto, 2014). The potential eruptions of
59 these volcanoes have raised concerns, with the Azumayama Volcano being one of the
60 most concerning of the active volcanoes in NE Japan. Azumayama is located in the Nasu
61 volcanic chain of the Quarternary volcanic front in NE Japan (Takahashi et al., 2013;
62 Yamamoto, 2005), and is composed of several andesitic edifices that have emerged since
63 the Pleistocene (Figure 1). Oana crater in the eastern part of Azumayama has active
64 fumaroles with recent maximum effusion rates of 600 tons/day. Oana crater brought on
65 the recent phreatic eruptions in 1977, 1952, and 1950 (Japan Meteorological Agency,
66 2013). Spontaneous seismic swarms have been reported beneath Azumayama since 2000,
67 and geodetic data of the global navigation satellite system (GNSS) baseline extensions

68 and of tilt changes accompanied those seismic swarms (Seki et al., 2020; Japan
69 Meteorological Agency, 2013; Yoshida et al., 2012). Although outstanding seismic
70 swarms were observed during 2014-2015 and 2018-2019 (Seki et al., 2020; Yoshigai et
71 al., 2019), no eruption has taken place so far.

72 For the eruption forecast, the shallower part beneath Azumayama down to a depth
73 of 0 km below sea level (depth is represented below sea level hereafter) is well
74 investigated (Seki et al., 2020; Yoshida et al., 2012). However, the transport and
75 distribution of magma/hydrothermal fluid in the 0-20 km depth range are unknown. This
76 depth range coincides with a seismicity gap: the volcano-tectonic earthquakes are
77 primarily restricted to depths of less than 1 km, and deep low-frequency tremors occur
78 below 20 km depth (Japan Meteorological Agency, 2013). Furthermore, magma
79 reservoirs beneath active volcanoes generally lie at depths of a few to 10 km (Chaussard
80 & Amelung, 2014), and any existing magma reservoir beneath Azumayama presumably
81 lies within this depth range. Takada & Fukushima (2013) model the low-viscosity ellipse
82 beneath Azumayama at -0.7-5.8 km depths from analysis of the interferometric synthetic
83 aperture radar (InSAR) data recording the subsidence of the edifice caused by the 2011

84 Tohoku-Oki Earthquake. Chen et al. (2018) image the slow shear wave velocity (V_s)
85 region at depths of 0 to 10 km around Azumayama using ambient noise tomography.
86 Those studies provide broad and blurred images of the magma reservoir. Geodetic data
87 locate the Mogi inflation sources at depths of 3 and 9 km beneath Oana crater (Seki et al.,
88 2020). The Mogi inflation sources probably show a more precise outline of the magma
89 reservoir.

90 Electrical resistivity (the reciprocal of conductivity) models beneath active
91 volcanoes using magnetotellurics (MT) have succeeded in exposing clear images of
92 magma reservoirs (Hata et al., 2018; Cordell et al., 2018; Aizawa et al., 2014; Bertland et
93 al., 2012; Heise et al., 2010; Hill et al., 2009). The primary purpose of this study is to
94 model the three-dimensional (3-D) resistivity distribution below Azumayama down to 20
95 km depth by MT, and we show the resultant resistivity model provides a clear image of
96 the magma reservoir beneath Azumayama. Along with defining the magma reservoir
97 from resistivity model, we discuss the petrological interpretation for the magma reservoir
98 and the threshold of a phreatic eruption of Azumayama.

99 The melt fraction and melt water content of magma reservoirs have been estimated

100 from resistivity models based on laboratory data of melt and rock resistivity (Laumonier
101 et al., 2017, 2015; Guo et al., 2017; Heise et al., 2016; Ichiki et al., 2015; McGary et al.,
102 2014). To gain more reliable quantitative interpretation of the magma reservoir, we
103 perform checker board resolution tests (CRTs) to estimate a confidence interval of
104 resistivity (CIR) of the magma reservoir image. This contributes to a more rigorous
105 quantitative interpretation of the magma reservoir in the petrological contexts from the
106 laboratory data.

107 Hydrothermal fluids exsolve from melts in the magma reservoir, and the ascent of
108 hydrothermal fluids often triggers phreatic eruptions. A key parameter controlling the
109 eruption triggering is permeability along the hydrothermal fluid pathway. At shallow
110 depths down to several hundred meters below the surface, clay minerals likely constitute
111 the primary impermeable layers suppressing the ascent of hydrothermal fluids. The
112 impermeable clay layers are imaged by MT as conductive bodies (Matsunaga et al., 2020;
113 Yoshimura et al., 2018; Tsukamoto et al., 2018; Komori et al., 2013). On the other hand,
114 densified magma on the pathway probably plays the impermeable role at higher
115 temperatures and deeper depths (Colombier et al., 2017; Kushnir et al., 2016; Heap et al.,

116 2015; Okumura & Sasaki, 2014). This study assumes this concept in which the densified
117 magma interrupts the ascent of hydrothermal fluids. The reduction of porosity and the
118 low hydrothermal fluid fraction resulting from the densification process produces a more
119 resistive image than the conductive hydrothermal fluids underlying the densified magma.
120 Although the theoretical relationship between the Kozeny-Carman equation
121 (permeability) and Archie's Law (resistivity) in porous media suggests that resistivity can
122 be converted into permeability, simple applications of the relationship are usually
123 misleading (Wright et al., 2009). Thus we estimate porosity (hydrothermal fluid fraction),
124 rather than permeability, of the impermeable region imaged as being resistive in
125 accordance with another relationship between resistivity and porosity, Hashin-
126 Shtrickman bound (Hashin & Shtrickman, 1962). On the basis of the estimated porosity
127 of the impermeable region, we test which index characterizes the impermeable region,
128 percolation threshold (e.g. Burgisser et al., 2017; Blower, 2001) or “change point” in
129 porosity-permeability relationship (Kushnir et al., 2016; Farquharson et al., 2015; Heap et
130 al., 2015, 2014). The index may be used as a potential diagnostic threshold for the forecast
131 of a phreatic eruption of Azumayama.

132 2. Methods, Data, and Analyses

133 2.1. Basic concept of method, data and data processing

134 MT and geomagnetic depth sounding (GDS) are resistivity exploration methods that
135 use the frequency response of electromagnetic (EM) field variation observed around the
136 Earth's surface. The frequency response varies with EM induction in the Earth induced
137 by external EM field variation. The frequency response and the EM induction reflect the
138 distribution of subsurface electrical resistivity. MT and GDS frequency responses, which
139 are impedance tensor and geomagnetic transfer functions, are defined as follows:

$$140 \quad (1) \begin{bmatrix} E_x^{obs}(f) \\ E_y^{obs}(f) \end{bmatrix} = \begin{bmatrix} Z_{xx}^{obs}(f) & Z_{xy}^{obs}(f) \\ Z_{yx}^{obs}(f) & Z_{yy}^{obs}(f) \end{bmatrix} \begin{bmatrix} H_x(f) \\ H_y(f) \end{bmatrix}$$

$$141 \quad (2) H_z(f) = A(f) H_x(f) + B(f) H_y(f)$$

142 where Z_{ij} ($i, j = x, y$): impedance tensor, A, B: geomagnetic transfer function, E_i ($i = x, y$),
143 H_i ($i = x, y, z$): Fourier spectrum of electric and magnetic field variation, subscript x, y, z :
144 north-south (N-S), east-west (E-W), down-up component, (f): function of frequency. The
145 impedance tensor contains galvanic distortion, a kind of observational site effect, which
146 affects the direct interpretation of raw observed impedance. The galvanic distortion is
147 expressed as:

$$148 \quad (3) \begin{bmatrix} Z_{xx}^{obs}(f) & Z_{xy}^{obs}(f) \\ Z_{yx}^{obs}(f) & Z_{yy}^{obs}(f) \end{bmatrix} = \begin{bmatrix} C_{xx} & C_{xy} \\ C_{yx} & C_{yy} \end{bmatrix} \begin{bmatrix} Z_{xx}^{inductive}(f) & Z_{xy}^{inductive}(f) \\ Z_{yx}^{inductive}(f) & Z_{yy}^{inductive}(f) \end{bmatrix}$$

149 C_{ij} ($i = x, y$) is galvanic distortion tensor. Note that C_{ij} is real and independent of frequency.

150 The distortion tensor cannot be fully corrected without performing additional,

151 cumbersome observations. Some researchers impose the correction by assuming spatial

152 smoothness or other constraints on the distortion tensor (Avdeeva et al., 2015). To cope

153 with the galvanic distortion, Caldwell et al. (2004) developed a distortion-free MT

154 parameter, the phase tensor, Φ :

$$155 \quad (4) \quad \Phi = X^{-1} Y = \begin{bmatrix} \Phi_{xx} & \Phi_{xy} \\ \Phi_{yx} & \Phi_{yy} \end{bmatrix}$$

$$156 \quad (5) \quad \begin{bmatrix} Z_{xx}^{obs}(f) & Z_{xy}^{obs}(f) \\ Z_{yx}^{obs}(f) & Z_{yy}^{obs}(f) \end{bmatrix} = \begin{bmatrix} X_{xx}(f) & X_{xy}(f) \\ X_{yx}(f) & X_{yy}(f) \end{bmatrix} + im \begin{bmatrix} Y_{xx}(f) & Y_{xy}(f) \\ Y_{yx}(f) & Y_{yy}(f) \end{bmatrix} = X + imY$$

157 where superscript -1: inverse matrix, im : imaginary number. The phase tensor indicates

158 the degree of subsurface resistivity heterogeneity (dimensionality) and the distortion-free,

159 equivalent one-dimensional (1-D) MT phase response. The phase tensor is diagonalized

160 to determine its principal axis using the horizontal axis rotation matrix, R :

$$161 \quad (6) \quad \Phi = R^T(\alpha-\beta) \Phi_{\min_max} R(\alpha+\beta)$$

$$162 \quad = \begin{bmatrix} \cos(\alpha - \beta) & -\sin(\alpha - \beta) \\ \sin(\alpha - \beta) & \cos(\alpha - \beta) \end{bmatrix} \begin{bmatrix} \Phi_{max} & 0 \\ 0 & \Phi_{min} \end{bmatrix} \begin{bmatrix} \cos(\alpha + \beta) & \sin(\alpha + \beta) \\ -\sin(\alpha + \beta) & \cos(\alpha + \beta) \end{bmatrix}$$

$$163 \quad (7) \quad \alpha = 1/2 \tan^{-1}((\Phi_{xy} + \Phi_{yx}) / (\Phi_{xx} - \Phi_{yy}))$$

$$164 \quad (8) \quad \beta = 1/2 \tan^{-1}((\Phi_{xy} - \Phi_{yx}) / (\Phi_{xx} + \Phi_{yy}))$$

165 Phase tensor ellipticity, \mathcal{A} , is defined as:

166 (9) $\mathcal{A} = (\Phi_{max} - \Phi_{min}) / (\Phi_{max} + \Phi_{min})$

167 The phase tensor is graphically represented by tensor ellipse (Heise et al., 2006). The

168 tensor principal axis represents eigenvalue and eigenvector, that is, tensor character

169 changes only in amplitude along the principal axis direction. Thus, the principal axis of

170 the phase tensor ellipse means that phase tensor element information in this direction is

171 not contaminated with information from other directions. Accordingly, the phase tensor

172 ellipse is represented by a circle ($\Phi_{max} = \Phi_{min}$) in 1-D, an elliptical shape ($\Phi_{max} \neq \Phi_{min}$) and

173 $\beta = 0$ in two-dimensions (2-D), and an ellipse and $\beta \neq 0$ in 3-D. The arc tangent of the

174 square root of the phase tensor determinant is considered to be the distortion-free

175 equivalent 1-D MT phase response around an observation site. The square root of phase

176 tensor determinant is denoted as Φ_2 :

177 (10) $\Phi_2 = \sqrt{\Phi_{xx}\Phi_{yy} - \Phi_{xy}\Phi_{yx}} = \sqrt{\Phi_{max}\Phi_{min}}$

178 GDS data are graphically represented by an induction vector. The Parkinson vector,

179 which is the most commonly used induction vector, points towards the conductor:

180 (11) In-phase: $-Re(A) \mathbf{e}_N - Re(B) \mathbf{e}_E$

181 (12) Quadrature-phase: $Im(A) \mathbf{e}_N + Im(B) \mathbf{e}_E$

182 where $\mathbf{e}_N, \mathbf{e}_E$ represents northward and eastward unit vector, respectively.

183 The MT and GDS data were acquired from 18 sites at Azumayama (Figure 1). The
184 study area is about 18 km N-S by 14 km E-W, with an average spacing between the sites
185 of 3.00 km. The EM field variation data were acquired with an MTU-5 system (Phoenix
186 Geophysics) at two sites during four days in September 2015, and at the other 16 sites in
187 September 2015 and 2017 using an ADU-07e system (Metronix Geophysics). All sites
188 recorded five-component EM field variations. The two-component horizontal telluric
189 field was observed using Pb-PbCl₂ electrodes with 40 m dipole lengths. The three-
190 component magnetic field for remote-reference processing was recorded at Okura village,
191 Yamagata prefecture (about 97 km north of Mt. Issaikyo) using the ADU-07 system, and
192 at Nishiwaga town, Iwate prefecture (about 210 km NNE of Mt. Issaikyo) using the MTU-
193 5A system. The MT and GDS frequency responses of the two sites were calculated from
194 0.00055 to 320 Hz using SSMT2K and MTEDITOR (Phoenix Geophysics), and for the
195 other 16 sites from 0.00012 to 384 Hz using BIRRP code (Chave & Thomson, 2004).

196 **2.2. Three-dimensional resistivity modeling**

197 The WSINV3DMT inversion code (Siripunvaraporn & Egbert, 2009) is used to

198 model the distribution of 3-D resistivity beneath Azumayama. The WSINV3DMT code
199 seeks an optimal model by minimizing the following objective function, W , using
200 Occam inversion algorithm (Constable et al., 1987):

$$201 \quad (13) \quad W(\mathbf{m}) = (\mathbf{m} - \mathbf{m}_0)^T \mathbf{C}_m^{-1} (\mathbf{m} - \mathbf{m}_0) + \lambda^{-1} (\mathbf{d} - \mathbf{F}[\mathbf{m}])^T \mathbf{C}_d^{-1} (\mathbf{d} - \mathbf{F}[\mathbf{m}])$$

202 \mathbf{m} : model parameter vector, \mathbf{m}_0 : prior model parameter vector (fixed in iteration), \mathbf{C}_m :
203 model covariance matrix, \mathbf{d} : data vector, \mathbf{C}_d : data covariance matrix, $\mathbf{F}[\]$: 3-D forward
204 operator, λ : Lagrange multiplier. The first and second terms are regularization and data
205 misfit, respectively. The λ is determined at each iteration stage so the normalized root-
206 mean-squared (RMS) misfit takes a minimum value. We call this Occam process. The
207 inversion data are real and imaginary parts of the MT impedance and GDS response at
208 18 periods, which have octaves between 1024, and 1.5625×10^{-2} , and 1.0417×10^{-2}
209 seconds. The number of data points is 3888 (18 sites \times 18 periods \times 12 responses). We
210 give 5 % of the MT impedance and 10 % of the GDS response data to the error floor. The
211 modeling space is 420 km \times 417 km \times 150 km, which is divided into $57 \times 59 \times 64$ blocks
212 in N-S, E-W and vertical directions. Resistivity of blocks in the marine area is fixed at
213 $0.3333 \Omega\text{m}$ and the SRTM30_PLUS model (Becker et al., 2009) is used to distinguish

214 seafloor. Land topography is incorporated into the model, and resistivity of air blocks
215 created by the land topography is fixed at $10^{12} \Omega\text{m}$. Each element of the model covariance
216 matrix, C_m , is imposed to follow a 1-D diffusion equation solution in each N-S, E-W and
217 vertical direction (Siripunvaraporn et al., 2005). The relaxation parameter $4\delta\tau$ (op. cit.) is
218 fixed at 2.0 in all three directions.

219 One inversion operation ends when the RMS misfit achieves a given threshold, or
220 when iteration, which means updating the Jacobian (strictly, $C_m \times \text{Jacobian}$), repeats a
221 given maximum iteration times. The RMS misfit of all data is defined as:

$$222 \quad (14) \quad \text{RMS misfit} = \sqrt{\frac{1}{N} (\mathbf{d} - \mathbf{F}[\mathbf{m}])^T \mathbf{C}_d^{-1} (\mathbf{d} - \mathbf{F}[\mathbf{m}])}$$

223 where N is number of data. The RMS misfit threshold and the maximum iteration times
224 are set to 1.0 and 10, respectively.

225 We start inversion using the initial prior model, where each marine, air, and
226 subsurface region is uniform, respectively. We test the four initial prior models, of which
227 the subsurface resistivities are 100, 300, 1000, and 3000 Ωm . If one inversion operation
228 completes in case where the RMS misfit achieved 1.0, the solution is accepted as a final
229 model. If one inversion operation completes the maximum number of iterations without

230 achieving the desired RMS, we replace the prior model into the best solution giving a
 231 minimum RMS misfit during the inversion operation (denoted as prior model update),
 232 and repeat another inversion operation. Once the best data misfit during the inversion
 233 operation do not significantly decrease compared with that during the previous inversion
 234 operation, the inversion stops and the solution is accepted as a final model. The F-test is
 235 employed to judge whether the data misfit significantly decreases or not. The test statistic
 236 F , defined below, follows an F-distribution with the degree of freedom (DOF) N and N :

$$237 \quad (15) \quad F = (\chi^2\text{-misfit}_{(i)}/N) / (\chi^2\text{-misfit}_{(i+1)}/N) = (\text{RMS misfit}_{(i)})^2 / (\text{RMS misfit}_{(i+1)})^2$$

238 where subscript i and $i+1$ means i -th and $(i+1)$ -th prior model update. The χ^2 -misfit in
 239 Equation 15 is defined as:

$$240 \quad (16) \quad \chi^2\text{-misfit} = (\mathbf{d}-\mathbf{F}[\mathbf{m}])^T \mathbf{C}_d^{-1} (\mathbf{d}-\mathbf{F}[\mathbf{m}]) = N \times (\text{RMS misfit})^2$$

241 We adopt the threshold 1.054, the 95 % confidence level of the left-tailed (or 5 %
 242 significance level of the right-tailed) F-test with DOF 3888 and 3888.

243 The best final model is selected from the four final models, each of which is
 244 originated from each of the four initial prior models.

245 To show the data misfit, we calculate misfit phase tensor representing differences

246 between two phase tensors. Two kinds of misfit phase tensor have been proposed: one by
 247 Peacock et al. (2012) and the other by Heise et al. (2007, 2008), and this study uses the
 248 misfit phase tensor of Peacock et al (2012). The misfit phase tensor of Peacock et al.
 249 (2012), $\Delta\Phi_{Peacock}$, and the misfit of the arithmetic mean of two principal axis magnitudes,
 250 $\Delta\Phi_{principal}$ are:

251 (17) $\Delta\Phi_{Peacock} = E - (\Phi_{obs}^{-1} \Phi_{cal})$

252 (18) $\Delta\Phi_{principal} = (|\Phi_{max}^{obs} - \Phi_{max}^{cal}| / \delta\Phi_{max} + |\Phi_{min}^{obs} - \Phi_{min}^{cal}| / \delta\Phi_{min}) / 2$

253 where E : 2×2 unit matrix, Φ_{obs} : observed phase tensor, Φ_{cal} : phase tensor calculated
 254 from resistivity model, Φ_{max}^{obs} , Φ_{min}^{obs} : two principal axis magnitudes of Φ_{obs} , Φ_{max}^{cal} ,
 255 Φ_{min}^{cal} : two principal axis magnitudes of Φ_{cal} , $\delta\Phi_{max}$, $\delta\Phi_{min}$: standard errors of two
 256 principal axis magnitudes of Φ_{obs} . Misfit phase tensor is graphically drawn in the same
 257 manner as a phase tensor. However, when an observed phase tensor has a large ellipticity,
 258 a large maximum principal axis often remains in both the Peacock et al.'s and Heise et
 259 al.'s misfit phase tensor ellipses, even if the data fit is fairly good. The reason we use
 260 Peacock et al.'s misfit phase tensor ellipse is the straightforward nature, that is, the
 261 maximum principal axis azimuth approaches $\alpha_{obs} + \beta_{obs} + \pi/2$ in a large ellipticity case as

262 the data fit gets better, while the Heise et al.'s misfit phase tensor ellipse has a rather
263 complex nature. We explain the detail in supplemental material 1.

264 **3. Results**

265 Figure 2 shows the observed $\tan^{-1}(\Phi_2)$ at various frequencies or periods. The $\tan^{-1}(\Phi_2)$
266 in the frequency range higher than 8.0 Hz has higher values in the area east of Oana
267 crater. The high $\tan^{-1}(\Phi_2)$ area assumes E-W elongation towards Oana crater. The $\tan^{-1}(\Phi_2)$
268 distribution typically shows N-S trends in the period range longer than 8.0 s, and
269 the $\tan^{-1}(\Phi_2)$ greater than 45° dominates in the western part of the area. The $\tan^{-1}(\Phi_2)$ falls
270 below 45° across the study area at 512 s period. These findings are consistent with the
271 final inversion resistivity model.

272 Figure 3 shows the RMS misfit in terms of prior model updates. The RMS misfits
273 in all inversion operations do not achieve 1.0. We obtain the final resistivity model at the
274 third prior model update starting with the initial prior model of 1000 Ωm subsurface. The
275 best RMS misfit is 2.42.

276 Figures 4 to 6 represent the results of the final resistivity model in plan or map view,
277 as a series of vertical profiles in the E-W direction, and as a similar series of vertical

278 profiles in the N-S direction. Figure 4 indicates the presence of three thin conductive
279 patches in the eastern part from Oana crater at a depth of 0.05 km. Those conductive
280 patches fade with increasing depth, and the E-W elongated conductor appears beneath
281 Oana crater at 3.50 km depth. The E-W elongated conductive feature extends down to a
282 depth of 5.50 km. The structure is delineated by the convex shape of the conductor in 3.5-
283 5.5 km depth range in the $C-C'$ profile of Figure 5. The Φ_2 response distribution in the
284 high frequency range (> 8.0 Hz) of the final resistivity model (Figure 2) also reveals this
285 feature. The conductor beneath Oana crater expands in the N-S direction at depths below
286 6 km. The plan view at 7.5 km depth in Figure 4 and the $H-H'$ profile in Figure 6 provide
287 clear images of the expansion. The Φ_2 distribution also shows this N-S trend at the middle
288 periods of 8.0 and 64 s (Figure 2). The area in the 7-9 km depth range below Oana crater
289 has the lowest resistivity value ($\sim 0.1 \Omega\text{m}$) in the final model, which also shows a second
290 conductive block between 5 and 10 km depth beneath Naka-azuma. The twin conductor
291 image can be found in the plan views at 7.50 and 9.50 km depth of Figure 4 and in the D -
292 D' profile of Figure 5. No apparent conductor is found below the observation sites at
293 depths greater than 20 km.

294 Figure 7 shows the observed and calculated phase tensor and misfit phase tensor
295 ellipses. The phase tensor ellipses across the study area have a large ellipticity in the
296 observed period bands. Because the phase tensor ellipticity is so great, some large
297 maximum principal axes remain for the misfit phase tensors. However, over half of these
298 align to the azimuth of $\alpha_{obs} + \beta_{obs} + \pi/2$. The data fits are reasonable in the middle period
299 range between 64 s and 32 Hz, while the misfit phase tensor ellipses show a poor data fit
300 at the 512 s period or longer. Details on the data fitting of MT apparent resistivity, phase
301 responses, and Parkinson vectors are presented in supplemental material 2.

302 **4. Resolution and Confidence Interval of Resistivity**

303 The better data misfit in the middle period range of 8-64 s indicates that the
304 conductive region at 3-15 km depth is well resolved. Focusing the conductor, we perform
305 the CRTs to investigate the resolution of the conductor on this observation condition, and
306 estimate CIR of the conductor.

307 Two CRTs are demonstrated, here. Figures 8-10 show the two checkerboard models
308 used to test whether the final model has 3 or 5 km resolution. The checkerboard is a single
309 layer, and background and checkbox resistivity is 1000 and 1 Ωm , respectively. The

310 marine and air blocks are fixed, as described in subsection 2.2. Synthetic datasets are
311 generated of the respective components at each site that are composed of MT impedance
312 and geomagnetic transfer functions with 5 % amplitude Gaussian noises. Because a
313 substantial amount of time and effort are required to demonstrate CRT replicating the
314 precise Occam process of the final model, the Lagrange multiplier, λ in Equation 13, is
315 fixed constant in the CRTs. The λ takes 0.10 at iteration 9 on the initial prior model, 0.10
316 at iteration 8 on the first update prior model, 0.032 at iteration 5 on the second update,
317 and 10 at iteration 2 on the third update, until we achieve the final model (cf. blue plots
318 in Figure 3). Here, we fix λ at 0.10 in the CRTs.

319 Figures 8 and 10 show the results of CRT using checkerboxes with dimensions of
320 about 3 km to a side. Outputs using each prior model shows blurred checkerboxes, and
321 the number of conductive checkerboxes cannot be properly determined. The northeastern
322 most output conductive checkbox moves horizontally from the original position, and
323 conductive checkbox resistivities are overestimated to be 5-10 Ωm or more. Figures 9
324 and 10 show the results from using checkerboxes with dimensions of about 5 km to a side.
325 While the conductive checkerboxes at depth inside the observation network are blurred,

326 the five conductive checkboxes could be distinguished. Moreover, the conductive
327 checkbox resistivities are properly estimated to be $1 \Omega\text{m}$ at the third update of the prior
328 model. The eight conductive checkboxes at depth outside the observation network are
329 hardly recognizable. These two CRTs reveal that the conductor at 5-10 km depth has no
330 resolution with the scale of less than 3 km, but reasonable resolution with the scale of
331 over 5 km.

332 We estimate the CIR of the conductor. The area of the conductor is defined as that
333 where the resistivity is less than 3 or $1 \Omega\text{m}$ between 3 and 15 km depth in the final model
334 (Figure 11). The horizontal dimension of the defined area is 15×20 km or 5×10 km.
335 The target area's resistivity is changed to a variety of constant values between 0.01 and
336 $100 \Omega\text{m}$, and the forward modeling is repeated to chase the data misfit change of each
337 site.

338 Figure 12 shows the F-statistics defined as Equation 15 for each of the 18 sites. Note
339 that total RMS misfit using all sites show no significant change in terms of the target
340 area's resistivity. The 95, 90, and 67 % confidence levels of left-tailed F-test with DOF
341 216 and 216 ($18 \text{ periods} \times 12 \text{ responses per site}$) are 1.252, 1.191, and 1.062 respectively.

342 As a result, the 90 and 67 % CIR of the under 3 Ωm area are estimated to be 0.02 \cong
343 (90 % CIR) \cong 70 Ωm and 0.3 \cong (67 % CIR) \cong 5 Ωm (Figure 12a). The RMS misfits
344 of some sites get significantly worse as the target area's resistivity decrease. The same
345 behavior also appears as the target area's resistivity increases. This nature enables both
346 the upper and lower bounds of CIR to be constrained. On the other hand, the CIR of the
347 area under 1 Ωm cannot be constrained using any of the 95, 90 and 67 % confidence
348 levels (Figure 12b). This is presumably due to the insufficient volume of the target area.
349 The integral equation formulation for the 3-D EM induction problem states that the
350 product of conductivity perturbation and volume, and distance between conductivity
351 perturbation (source) and a site (receiver) primarily controls the EM field and impedance
352 response changes at the site (Hohman, 1975; Wannamaker et al., 1984; Zhdanov et al.,
353 2006). Note that less distance between the source and the receiver produces larger Green
354 functions of EM fields.

355 **5. Discussion**

356 **5.1. Comparisons with other geophysical results and other active volcanoes**

357 The conductive image at the 3-15 km depth range is consistent with the slow Vs
358 region by ambient noise tomography (Chen et al., 2018), although the core of the slow

359 velocity region is located several km to the west. The low viscosity ellipsoid body inferred
360 with the InSAR data recording subsidence around Azumayama caused by the 2011
361 Tohoku-Oki Earthquake (Takada & Fukushima, 2013) is partly overlapped with the
362 conductor, which lies at a shallower depth range (−0.7 to 5.8 km depth). The electrical
363 model gives a more focused image than the slow velocity and low viscosity models.

364 GNSS baseline length and tilt changes around Azumayama accompanied by recent
365 volcanic activities have revealed the presence of the Mogi inflation source deeper than 2
366 km beneath Oana crater. Seki et al. (2020) propose the two and three Mogi inflation
367 source models by analyzing the data of the tilt meter located about 800 m ESE of Oana
368 crater and 16 GNSS sites during the volcanic activity in May 2018 to April 2019. Figure
369 13 shows the Mogi model inflation source models superimposed on the final resistivity
370 model. The inflation source at 2.7 or 3.7 km depth lies in the resistive side near the top
371 boundary of the conductor. The resistivity around the inflation source is 30-300 Ωm .
372 Although it is hard to evaluate the CIR of the area around the inflation source, the lower
373 bound of the CIR could be taken as the upper bound of the CIR of the conductor estimated
374 in the previous section. On the other hand, the source at 9 km depth from the Mogi

375 inflation source model is located inside the conductor. However, this Mogi source
376 location is determined with an accuracy of a few km. This Mogi source likely becomes
377 compressive occasionally. The tilt meter located about 11 km south of Oana crater
378 showed a declining trend in the direction toward Oana crater during the volcanic tremors
379 on 22 July, 2019 (Yoshigai et al., 2019). The compression source of the tilt change is
380 located at about 10 km depth beneath Oana crater (Yoshigai and Nihara, priv. comm.),
381 which likely coincides with the inflation source at 9 km depth of the three Mogi inflation
382 source model.

383 Similar conductors beneath other active volcanoes are found at depths of 3-15 km
384 (e.g. Aso: Hata et al., 2018; Laguna del Maule: Cordell et al., 2018; Kirishima: Aizawa
385 et al., 2014; Taupo: Bertland et al., 2012, Heise et al., 2010; Mt. Adams and St. Helens:
386 Hill et al., 2009). Melt inclusion samples from active volcanoes show that magma
387 reservoirs generally lie at depth ranges of a few km to 13 km (Cashman et al., 2017).
388 According to the compilation by Chaussard & Amelung (2014), magma reservoir depths
389 in arc volcanoes are a few to 10 km deep, and correlate with crustal thickness and age.
390 Thus, the conductor beneath Oana crater is interpreted as the magma reservoir comprising

391 magma, hydrothermal fluid, and rock complexes.

392 **5.2. Melt fraction of the magma reservoir**

393 We interpret that the shallower part of the conductor or the magma reservoir (down
394 to 4 or 5 km) is composed of dacitic melt-rock-hydrothermal fluid complex. Geothermal
395 gradients of over 75-100 K/km around Azumayama (Tanaka et al., 2004) indicate
396 geotherms above the solidus of silicic melts at greater depths than 4 or 5 km, and melts
397 may exist in the magma reservoir. The phenocrysts in the andesite and basaltic andesite
398 samples of Oana unit are divided into mafic, mixed magma-derived, and felsic silicates
399 (Ban et al., 2016). The felsic phenocrysts have the shallowest origin, which is dacitic melt
400 with water contents of 2.75-3.25 wt % at about 4 km depth by Rhyolite-MELTS analysis,
401 and at 880-890 °C by pyroxene geothermometry (op. cit.). The 4 km depth is near the top
402 of the conductor. Hence, we first assume the shallower part of the conductor is composed
403 of two phases of dacitic melt and rock. The melt water content can range up to the water
404 saturated condition of 5.5 wt % (Wallace, 2005; Sisson and Bacon, 1999). Based on recent
405 laboratory data of dacitic melt resistivity and modified Archie's Law with $m=1.05$
406 (Laumonier, et al., 2015), we calculate bulk resistivity for the dacitic melt and rock
407 complex at 900 °C and 4 km depth (0.15 GPa). Figure 14 compares the bulk resistivity

408 and the 67 % CIR (0.3 to 5 Ω m) at various water contents. While the upper bound of 67 %
409 CIR beneath Oana crater corresponds to the complex with a melt fraction of 0.22 to 0.63
410 at water contents of 5.5 to 3.5 wt %, the complex with any reasonable melt and water
411 content cannot explain the lower bound of 67 % CIR. Hydrothermal fluids and/or mafic
412 melts are more or less required to explain the lower bound of 67 % CIR (see also
413 Laumonier et al., 2015). Regarding the shallower part of the magma reservoir where the
414 magma differentiation is mature, hydrothermal fluids rather than mafic melts are the
415 probable interpretation for this discrepancy.

416 Magma mixing and differentiation probably occur in the magma reservoir (e.g.
417 Takahashi et al., 2013; Yoshida et al., 2014; Tatsumi et al., 2008; Kimura & Yoshida,
418 2006; Toya et al., 2005), and result in the magma reservoir becoming increasingly more
419 mafic with depth. Thus, we consider more mafic condition, an andesitic melt and rock
420 complex at a deep depth inside the conductor. Figure 15 shows the bulk resistivity of the
421 complex at 900 °C, and 9 km depth (0.29 GPa), with the melt water contents up to 8 wt %
422 of water saturation (op. cit.). The modified Archie's Law with $m=1.05$ is used with
423 andesitic melt resistivity models by Guo et al. (2017) and Laumonier et al. (2017). The

424 upper bound of 67 % CIR is explained by the complex with a melt fraction of 0.04 to 0.76
425 at water contents of 8.0 to 4.0 wt %. The lower boundary corresponds to the complex
426 with a melt fraction of 0.61 (Guo et al.'s model) or 0.84 (Laumonier et al.'s model) with
427 almost the water saturation. A melt with the water content lower than 8.0 wt % cannot
428 explain the lower bound. Meanwhile, the Mogi inflation/compression source is likely
429 located in 9-10 km depth range. Although the accuracy of the Mogi source location is a
430 few km, we assume the Mogi source lies inside the conductor. The viscosity of a melt and
431 rock complex is a function of the melt fraction. The viscosity abruptly changes around
432 melt fractions of 0.4. The complex with a melt fraction of less than 0.4 is defined as mush.
433 The deformation of mush is under the control of crystalline or solid framework rather
434 than that of melt (Cashman et al., 2017, and references herein). Hence, the Mogi source
435 must lie in the mush, assuming that the Mogi source is located inside the magma reservoir.
436 The melt fraction of 0.4 and melt water content of 8 wt % results in 0.47 or 0.73 Ωm ,
437 which almost explains the lower bound of 67 % CIR. Consequently, the magma
438 reservoir's resistivity with 67 % CIR may be explained by a water-saturated andesitic melt.
439 However, if we consider the safer 90 %, even higher pressure condition (the conductor

440 bottom ~15 km depth) and greater water content (~ 10 wt %) cannot explain the lower
441 bound (0.02 Ωm) of the 90 % CIR.

442 **5.3. Interruption of hydrothermal fluid ascent**

443 The shallower part of the magma reservoir is composed of the dacitic melt-rock-
444 hydrothermal fluid complex. Although hydrothermal fluids exsolve from the dacitic melt
445 near the top of the magma reservoir, an impermeable wall and conduit prevent the
446 hydrothermal fluids from ascending and causing a phreatic eruption. The Mogi inflation
447 source at 2.7 or 3.7 km depth near the top of the conductor indicates the spot of the
448 interruption. The impermeable wall and conduit results from porosity reduction through
449 magma densification (Heap et al., 2015; Okumura & Sasaki, 2014). The densification
450 presumably has reached the percolation threshold in porosity (e.g. Burgisser et al., 2017;
451 Blower, 2001) or the "change point" porosity in the permeability-porosity relationship
452 (Heap et al., 2014, 2015; Farquharson et al., 2015; Kushnir et al., 2016). We test which
453 index gives the consistent explanation for the resistivity of the impermeable region,
454 percolation threshold or change point. The change point porosity is reported to be 10 to
455 15 vol % (op. cit.). On the other hand, the percolation threshold varies depending on the
456 conditions such as the transition between explosive and effusive eruptions, the inherent

457 hysteresis between prograde and retrograde periods, and others (e.g. Burgisser et al.,
458 2017; Colombier et al. 2017; Rust & Cashman 2011; Michaut et al., 2009; Muller, et al.,
459 2005; Rust & Cashman, 2004). We consider the general percolation threshold for effusive
460 eruption, 5 %, and for explosive eruption, 30 % (Colombier et al., 2017; Muller et al.,
461 2005). The impermeable region means the Mogi inflation source region at 2.7 or 3.7 km
462 depth in this context. As mentioned in subsection 5.1, we take the lower bound of the CIR
463 at the Mogi inflation source as the upper bound of the CIR for the magma reservoir's
464 conductor.

465 Figure 16 shows the bulk resistivity of two phases (hydrothermal fluid-rock) as a
466 function of the hydrothermal fluid fraction. The Hashin-Shtrickman upper bound in
467 conductivity (Hashin & Shtrickman, 1962) is used as mixing law, because of no
468 information about m in modified Archie's Law on this two phase complex. The
469 hydrothermal fluid is assumed to be supercritical with a resistivity of 0.3 to 0.1 Ωm at
470 conditions of 750-900 $^{\circ}\text{C}$, 0.13-0.15 GPa, and nearly saturated with CO_2 exsolution
471 (Nesbitt, 1993; Marshall & Frantz, 1987). Most combinations of the lower bound of CIR
472 and hydrothermal fluid resistivity suggest that the hydrothermal fluid fraction has less

473 than 5 % of percolation threshold porosity at the inflation source. Thus, the percolation
474 threshold porosity in an effusive eruption probably characterizes the impermeable wall
475 and conduit associated with the Mogi inflation source at 2.7 or 3.7 km depth. Assuming
476 0.3 Ωm for hydrothermal fluid resistivity and 5 Ωm for the lower bound of the CIR, the
477 hydrothermal fluid fraction at the inflation source has porosity over the percolation
478 threshold for effusive eruption and below the change point. The change point porosity
479 could be the threshold that characterizes the permeability causing the Mogi inflation
480 source.

481 **6. Conclusions**

482 Our 3-D resistivity model shows a clear conductive image of a magma reservoir
483 beneath Oana crater of Azumayama Volcano at depths of 3 to 15 km. The horizontal
484 dimension of the less than 3 Ωm conductor is 15 to 20 km. The 67 % and 90 % CIR of
485 the conductor is 0.3 to 5 and 0.02 to 70 Ωm , respectively. The confidence interval is
486 estimated by using a F-test to evaluate the RMS misfit change of each site with changes
487 in the conductor's resistivity. The CRTs suggest the dataset can resolve a conductive body
488 over 5 km in scale with unbiased resistivity at depths of 5 to 10 km. The image of the

489 conductive magma reservoir by the final resistivity model overlapped with the low
490 viscosity model from InSAR data (Takada & Fukushima, 2013) and the slow Vs region
491 determined by ambient noise tomography (Chen et al., 2018). The Mogi inflation sources
492 derived from GNSS and tilt data are located near the top boundary of the magma
493 reservoir's conductor at 2.7 or 3.7 km depth, and inside the conductor at 9 km depth. The
494 shallower part of the magma reservoir is interpreted as a water-saturated, dacitic melt-
495 silicic rock-hydrothermal fluid complex. The hydrothermal fluids appear necessary,
496 because the lower boundary of the confidence interval for resistivity cannot be explained
497 by a water-saturated (5.5 wt %) dacitic melt alone. The deeper part of the conductor is
498 interpreted as a water-saturated (8 wt %) andesitic melt-mafic rock complex. Assuming
499 that the Mogi inflation source at 2.7 or 3.7 km depth indicates the interruption of
500 hydrothermal fluid ascent, the porosity or hydrothermal fluid fraction at the Mogi
501 inflation source is estimated to be generally below 5 % of the percolation threshold in the
502 effusive eruption case. Depending on the CIR at the Mogi inflation source and resistivity
503 of hydrothermal fluid, the change point of porosity-permeability, rather than the
504 percolation threshold, might characterize the permeability resulting in the Mogi source.

505 The model shows no lower crust (20 to 35 km depth) conductor, and no correlation
506 between the conductor beneath Oana crater and deep, low-frequency tremors. This may
507 be due to the use of MT data in a period range shorter than 1024 s. Longer-period MT
508 data will probably reveal the lower crust conductor.
509

510 **Declarations**

511 **Ethics approval and consent to participate**

512 Not applicable

513 **Consent for publication**

514 Not applicable

515 **List of abbreviations**

516 1-D, 2-D, 3-D: one-dimensional, two-dimensional, three-dimensional

517 CIR: confidence interval of resistivity

518 CRT: checkerboard resolution test

519 DOF: degree of freedom

520 EM: electromagnetic

521 GDS: geomagnetic depth soundings

522 GNSS: global navigation satellite system

523 InSAR: interferometric synthetic aperture radar

524 MT: magnetotellurics

525 NE, NNE: northeast(ern), north-north-east(ern)

526 N-S, E-W: north-south, east-west

527 RMS: root-mean-squared

528 Vs: shear wave velocity

529 **Availability of data and materials**

530 The data are available through corresponding author by request.

531 **Competing interests**

532 The authors have no competing interests.

533 **Funding**

534 This study is supported by the Ministry of Education, Culture, Sports, Science and

535 Technology (MEXT) of Japan, under the Program of Mobile and Intensive Observation-

536 Research System Integration for Volcanic Areas, and the Earthquake and Volcano

537 Hazards Observation and Research Program (Earthquake and Volcano Hazard Reduction

538 Research).

539 **Authors' contributions**

540 MI performed MT data acquisition, all analyses, discussion, wrote the manuscript

541 and created the figures. TK, TN performed MT data acquisition. SM, MY planned the

542 project. YM proposed the project and obtained funding. MU prepared and calibrated the

543 magnetotelluric equipment, and contributed to the discussion.

544 **Acknowledgements**

545 We are grateful to Satoshi Okumura, Masao Ban, Yu Nihara, Yusuke Yoshigai, Jun

546 Okada, Yo Fukushima, and the staff of Sendai Regional Headquarters of Japan

547 Meteorological Agency for valuable comments and discussion. We thank Koki Aizawa

548 for providing the operation techniques of ADU-07e. Urabandai Environment Ranger

549 Office, Fukushima and Yonezawa City Office, and Fukushima and Aizu Forest Office

550 facilitated the observation. Geothermal Energy Research and Development Co. Ltd. and

551 Nittetsu Mining Consultants Co. Ltd. kindly provided the remote reference data. Figures

552 are created using Generic Mapping Tools and Paraview Software.

553

554 **References**

- 555 Aizawa, K., et al., (2014), Three-dimensional resistivity structure and magma plumbing
556 system of the Kirishima Volcanoes as inferred from broadband magnetotelluric data, J.
557 Geophys. Res. Solid Earth, 119, 198-215, doi:10.1002/2013JB010682
- 558 Avdeeva, A., Moorkamp, M., Avdeev, D., Jegen, M., Miensopust, M., (2015), Three-
559 dimensional inversion of magnetotelluric impedance tensor data and full distortion matrix,
560 Geophys. J. Inter., 202, 464-481, doi: 10.1093/gji/ggv144
- 561 Ban, M., Takebe, Y., Adachi, T., Matsui, R., Nishi, Y., (2016), Eruption histories of Zao
562 and Azuma Volcanoes and their magma feeding systems for recent activities, Bull. Earthq.
563 Res. Inst., Univ. Tokyo, 91, 25-39
- 564 Bebbington, M. S., and Marzocchi, W., (2011), Stochastic models for earthquake
565 triggering of volcanic eruptions, J. Geophys. Res. Solid Earth, 116, B05204,
566 doi:10.1029/2010JB008114
- 567 Becker, J. J., et al., (2009), Global Bathymetry and Elevation Data at 30 Arc Seconds
568 Resolution: SRTM30_PLUS, Marine Geodesy, 32, 355-371, doi:
569 10.1080/01490410903297766
- 570 Bertland, E. A., et al., (2012), Magnetotelluric imaging of upper-crustal convection

571 plumes beneath the Taupo Volcanic Zone, New Zealand, *Geophys. Res. Lett.*, 39, L02304,
572 doi:10.1029/2011GL050177

573 Blower, J., (2001), Factors controlling permeability-porosity relationships in magma.
574 *Bull. Volcanol.*, 63, 497-504. doi: 10.1007/s004450100172

575 Burgisser, A., Chevalier, L., Gardner, J. E., Castro, J. M., (2017), The percolation
576 threshold and permeability evolution of ascending magmas, *Earth Planet. Sci. Lett.*, 470,
577 37-47, doi: 10.1016/j.epsl.2017.04.023

578 Caldwell, T. G., Bibby, H. M., Brown, C., (2004), The magnetotelluric phase tensor,
579 *Geophys. J. Inter.*, 158, 457-469, doi: 10.1111/j.1365-246X.2004.02281.x

580 Cashman, K. V., Sparks, R. S. J., Blundy, J. D., (2017), Vertically extensive and unstable
581 magmatic systems: A unified view of igneous processes, *Science*, 355, 6331, eaag3055,
582 doi: 10.1126/science.aag3055

583 Chaussard, E., and Amelung, F., (2014), Regional controls on magma ascent and storage
584 in volcanic arcs, *Geochem. Geophys. Geosyst.*, 15, 1407-1418,
585 doi:10.1002/2013GC005216

586 Chave, A. D., and Thomson, D. J., (2004), Bounded influence magnetotelluric response

587 function estimation, *Geophys. J. Inter.*, 157, 988-1006, doi:10.1111/j.1365-
588 246X.2004.02203.x

589 Chen, K.-X., Gung, Y., Kuo, B.-Y., Huang, T.-Y., (2018), Crustal magmatism and
590 deformation fabrics in northeast Japan revealed by ambient noise tomography. *J. Geophys.*
591 *Res. Solid Earth*, 123, 8891-8906, doi: 10.1029/2017JB015209

592 Colombier, M., et al., (2017), The evolution of pore connectivity in volcanic rocks, *Earth*
593 *Planet. Sci. Lett.*, 462, 99-109, doi: 10.1016/j.epsl.2017.01.011

594 Constable, S. C., Parker, R. L., Constable, C. G., (1987), Occam's inversion; a practical
595 algorithm for generating smooth models from electromagnetic sounding data, *Geophys.*,
596 52, 289-300, doi: 10.1190/1.1442303

597 Cordell, D., Unsworth, M. J., Diaz, D., (2018), Imaging the Laguna del Maule volcanic
598 field, central Chile, using magnetotellurics: Evidence for crustal melt regions laterally-
599 offset from surface vents and Holocene lava flows. *Earth Planet. Sci. Lett.*, 488, 168-180,
600 doi: 10.1016/j.epsl.2018.01.007

601 Farquharson, J., Heap, M. J., Varley, N. R., Baud, P. Reuschle, T., (2015), Permeability
602 and porosity relationships of edifice-forming andesites: A combined field and laboratory

603 study, *J. Volcanol. Geotherm. Res.*, 297, 52-68, doi:10.1016/j.jvolgeores.2015.03.016

604 Guo, X., Li, B., Ni, H., Mao, Z., (2017), Electrical conductivity of hydrous andesitic melts
605 pertinent to subduction zones, *J. Geophys. Res. Solid Earth*, 122, 1777-1788,
606 doi:10.1002/2016JB013524

607 Hashin, Z., and Shtrikman, S., (1962), A variational approach to the theory of effective
608 magnetic permeability of multiphase materials: *J. Appl. Phys.*, 33 (10), 3125-3131, doi:
609 10.1063/1.1728579

610 Hata, M., Matsushima, N., Takakura, S., Utsugi, M., Hashimoto, T., Uyeshima, M.,
611 (2018), Three-dimensional electrical resistivity modeling to elucidate the crustal magma
612 supply system beneath Aso caldera, Japan. *J. Geophys. Res. Solid Earth*, 123, 6334-6346,
613 doi: 10.1029/2018JB015951

614 Heap, M.J., Farquharson, J.I., Wadsworth, F.B., Kolzenburg, S., Russell, J.K., (2015),
615 Timescales for permeability reduction and strength recovery in densifying magma, *Earth*
616 *Planet. Sci. Lett.*, 429, 223-233, doi: 10.1016/j.epsl.2015.07.053

617 Heap, M. J., et al., (2014), Microstructural controls on the physical and mechanical
618 properties of edifice-forming andesites at Volcán de Colima, Mexico, *J. Geophys. Res.*

619 Solid Earth, 119, 2925-2963, doi:10.1002/2013JB010521

620 Heise, W., et al., (2016), Imaging the deep source of the Rotorua and Waimangu
621 geothermal fields, Taupo Volcanic Zone, New Zealand, J. Volcanol. Geotherm. Res., 314,
622 39-48, doi: 10.1016/j.jvolgeores.2015.10.017

623 Heise, W., Caldwell, T. G., Bibby, H. M., Bennie, S. L., (2010), Three-dimensional
624 electrical resistivity image of magma beneath an active continental rift, Taupo Volcanic
625 Zone, New Zealand, Geophys. Res. Lett., 37, L10301, doi:10.1029/2010GL043110

626 Heise, W., Caldwell, T. G., Bibby, H. M., Bannister, S. C., (2008), Three-dimensional
627 modelling of magnetotelluric data from the Rotokawa geothermal field, Taupo Volcanic
628 Zone, New Zealand, Geophys. J. Inter., 173, 740-750, doi: 10.1111/j.1365-
629 246X.2008.03737.x

630 Heise, W., et al., (2007), Melt distribution beneath a young continental rift: The Taupo
631 Volcanic Zone, New Zealand, Geophys. Res. Lett., 34, L14313,
632 doi:10.1029/2007GL029629

633 Heise, W., Caldwell, T. G., Bibby, H.M., Brown, C., (2006), Anisotropy and phase splits
634 in magnetotellurics, Phys. Earth Planet. Interior, 158, 107-121, doi:

635 10.1016/j.pepi.2006.03.021

636 Hill, G. J., et al., (2009), Distribution of melt beneath Mount St Helens and Mount Adams
637 inferred from magnetotelluric data, *Nature Geosci*, 2, 785-789, doi:10.1038/ngeo661

638 Hohmann, G. W., (1975), Three-dimensional induced polarization and electromagnetic
639 modeling, *Geophys.*, 40, 309-324, doi: 10.1190/1.1440527

640 Ichiki, M., et al., (2015), Electrical image of subduction zone beneath northeastern Japan,
641 *J. Geophys. Res. Solid Earth*, 120, 7937-7965, doi:10.1002/2015JB012028

642 Ikegaya, T., and Yamamoto, M., (2020), Spatio-temporal characteristics and focal
643 mechanisms of deep low-frequency earthquakes beneath Zao volcano, Japan, In:
644 Abstracts of 2020 EGU General Assembly, EGU2020-12533, doi: 10.5194/egusphere-
645 egu2020-12533

646 Japan Meteorological Agency, (2013), Azumayama. In: Japan Meteorological Agency,
647 The Volcanological Society of Japan (ed.) National catalogue of the active volcanoes in
648 Japan, 4th ed. Japan Meteorological Agency, Tokyo,
649 https://www.data.jma.go.jp/svd/vois/data/tokyo/STOCK/souran_eng/volcanoes/034_azumayama.pdf
650

651 Kariya, K. A., and Shankland, T. J., (1983), Electrical conductivity of dry lower crustal
652 rocks. *Geophys.*, 48 (1), 52-61, doi:10.1190/1.1441407

653 Kimura, J., and Yoshida, T., (2006), Contributions of Slab Fluid, Mantle Wedge and Crust
654 to the Origin of Quaternary Lavas in the NE Japan Arc, *J. Petrol.*, 47, 2185-2232,
655 doi:10.1093/petrology/egl041

656 Komori, S., Kagiya, T., Utsugi, M., Inoue, H., Azuhata, I., (2013), Two-dimensional
657 resistivity structure of Unzen Volcano revealed by AMT and MT surveys, *Earth Planets
658 Space*, 65, 759-766, doi: 10.5047/eps.2012.10.005

659 Koyama, J., (2015), Is it true that great earthquakes induce large volcanic eruptions
660 worldwide?, *Geophys. Bull. Hokkaido Univ.*, 78, 53-68, doi: 10.14943/gbhu.78.53

661 Kushnir, A. R. L., et al., (2016), Probing permeability and microstructure: Unravelling
662 the role of a low-permeability dome on the explosivity of Merapi (Indonesia), *J. Volcanol.
663 Geotherm. Res.*, 316, 56-71, doi: 10.1016/j.jvolgeores.2016.02.012

664 Laumonier, M., Gaillard, F., Muir, D., Blundy, J., Unsworth, M., (2017), Giant magmatic
665 water reservoirs at mid-crustal depth inferred from electrical conductivity and the growth
666 of the continental crust, *Earth Planet. Sci. Lett.*, 457, 173-180, doi:

667 10.1016/j.epsl.2016.10.023

668 Laumonier, M., Gaillard, F., Sifre, D., (2015), The effect of pressure and water
669 concentration on the electrical conductivity of dacitic melts: implication for

670 magnetotelluric imaging in subduction areas, *Chem. Geol.*, 418, doi:

671 10.1016/j.chemgeo.2014.09.019

672 Marshall, W. L., and Frantz, J. D., (1987), Electrical conductance measurements of dilute,
673 aqueous electrolytes at temperatures to 800°C and pressures to 4000 bars: Techniques and

674 interpretations, In: Barnes, H. L., Ulmer, G. C. (Eds.), *Hydrothermal Experimental*
675 *Techniques*, Wiley-Interscience, Chap. 11, 261-292

676 Matsunaga, Y., et al., (2020), Magmatic hydrothermal system inferred from the resistivity
677 structure of Kusatsu-Shirane Volcano, *J. Volcanol. Geotherm. Res.*, 390, 106742, doi:

678 10.1016/j.jvolgeores.2019.106742

679 McGary, R. S., Evans, R. L., Wannamaker, P. E., Elsenbeck, J., Rondenay, S., (2014),
680 Pathway from subducting slab to surface for melt and fluids beneath Mount Rainier,

681 *Nature*, 511, 338-341, doi:10.1038/nature13493

682 Michaut, C., Bercovici, D., Sparks, R. S. J., (2009), Ascent and compaction of gas rich

683 magma and the effects of hysteretic permeability, *Earth Planet. Sci. Lett.*, 282(1-4), 258-
684 267, doi: 10.1016/j.epsl.2009.03.026

685 Mueller, S., Melnik, O., Spieler, O., Scheu, B., Dingwell, D. B., (2005), Permeability and
686 degassing of dome lavas undergoing rapid decompression: An experimental
687 determination, *Bull. Volcanol.*, 67 (6), 526-538, doi: 10.1007/s00445-004-0392-4

688 Nesbitt, B. E., (1993), Electrical resistivities of crustal fluids, *J. Geophys. Res.*, 98 (B3),
689 4301-4310, doi: 10.1029/92JB02576

690 Nishimura, T., (2017), Triggering of volcanic eruptions by large earthquakes, *Geophys.*
691 *Res. Lett.*, 44, 7750-7756, doi: 10.1002/2017GL074579

692 Okumura, S., and Sasaki, O., (2014), Permeability reduction of fractured rhyolite in
693 volcanic conduits and its control on eruption cyclicity, *Geology*, 42, 843-846, doi:
694 10.1130/G35855.1

695 Peacock, J. R., Thiel, S., Reid, P., Heinson, G., (2012), Magnetotelluric monitoring of a
696 fluid injection: Example from an enhanced geothermal system, *Geophys. Res. Lett.*, 39,
697 L18403, doi: 10.1029/2012GL053080

698 Rust, A. C., and Cashman, K. V., (2011), Permeability controls on expansion and size

699 distributions of pyroclasts, *J. Geophys. Res. Solid Earth*, 116, B11202,
700 doi:10.1029/2011JB008494.

701 Rust, A. C., and Cashman, K. V., (2004), Permeability of vesicular silicic magma: inertial
702 and hysteresis effects, *Earth Planet. Sci. Lett.*, 228, 93-107, doi:
703 10.1016/j.epsl.2004.09.025

704 Seki, S., et al., (2020), Volcanic Activity in 2018-19 at Azumayama Volcano, Japan, *Quart.*
705 *J. Seismology* (revised)

706 Siripunvaraporn, W., and Egbert, G. D., (2009), WSINV3DMT: Vertical magnetic field
707 transfer function inversion and parallel implementation, *Phys. Earth Planet. Int.*, 173,
708 317-329, doi: 10.1016/j.pepi.2009.01.013

709 Siripunvaraporn, W., Egbert, G. D., Lenbury, Y., Uyeshima, M., (2005), Three-
710 dimensional magnetotelluric inversion: data-space method, *Phys. Earth Planet. Inter.*, 150,
711 3-14, doi: 10.1016/j.pepi.2004.08.023

712 Sisson, T. W., and Bacon, C. R., (1999), Gas-driven filter pressing in magmas, *Geology*,
713 27 (7), 613-616, doi: 10.1130/0091-7613(1999)027<0613:GDFPIM>2.3.CO;2

714 Takada, Y., and Fukushima, Y., (2013), Volcanic subsidence triggered by the 2011 Tohoku

715 earthquake in Japan, *Nature Geosci*, 6, 637-641, doi:10.1038/ngeo1857

716 Takahashi, T., et al., (2013), Primary Magmas at the Volcanic Front of the NE Japan Arc:
717 Coeval Eruption of Crustal Low-K Tholeiitic and Mantle-derived Medium-K Calc-
718 Alkaline Basalts at Azuma Volcano, *J. Petrol.*, 54 (1), 103-148, doi:
719 10.1093/petrology/egs065

720 Tanaka, A., Yamano, M., Yano, Y., Sasada, M., (2004), Geothermal gradient and heat flow
721 data in and around Japan (I): Appraisal of heat flow from geothermal gradient data, *Earth*
722 *Planet Space*, 56, 1191-1194, doi: 10.1186/BF03353339

723 Tatsumi, Y., et al., (2008), New Insights into Andesite Genesis: the Role of Mantle-
724 derived Calc-alkalic and Crust-derived Tholeiitic Melts in Magma Differentiation
725 beneath Zao Volcano, NE Japan, *J. Petrol.*, 49, 1971-2008, doi: 10.1093/petrology/egn055

726 Toya, N., Ban, M., Shinjo, R., (2005), Petrology of Aoso volcano, northeast Japan arc:
727 temporal variation of the magma feeding system and nature of low-K amphibole andesite
728 in the Aoso-Osore volcanic zone, *Contrib Mineral Petrol*, 148, 566-581, doi:
729 10.1007/s00410-004-0621-z

730 Tsukamoto, K., et al., (2018), Three-dimensional resistivity structure of Iwo-yama

731 volcano, Kirishima Volcanic Complex, Japan: relationship to shallow seismicity, surface
732 uplift, and a small phreatic eruption. *Geophys. Res. Lett.* 45, 12821-12828, doi:
733 10.1029/2018GL080202

734 Wallace, P. J., (2005), Volatiles in subduction zone magmas: concentrations and fluxes
735 based on melt inclusion and volcanic gas data, *J. Volcanol. Geotherm. Res.*, 140, 217-
736 240, doi: 10.1016/j.jvolgeores.2004.07.023

737 Wannamaker, P. E., Hohmann, G. W., Ward, S. H., (1984), Magnetotelluric responses of
738 three-dimensional bodies in layered earths, *Geophys.*, 49, 1517-1533, doi:
739 10.1190/1.1441777

740 Wright, H. M.N., Cashman, K. V., Gottesfeld, E. H., Roberts, J. J., (2009), Pore structure
741 of volcanic clasts: Measurements of permeability and electrical conductivity, *Earth Planet.*
742 *Sci. Lett.*, 280, 93-104, doi: 10.1016/j.epsl.2009.01.023

743 Yamamoto, M., (2014), Volcanic activities of Hakkoda volcano after the 2011 Tohoku-
744 Oki earthquake, In: Abstracts of 2014 Japan Geoscience Union Meetings, SVC55-P06e,
745 Yokohama, Japan, 28 April to 2 May 2014

746 Yamamoto, T., (2005), Eruptive history of Azuma volcano, NE Japan during last 7000

747 years: Stratigraphy and magma-plumbing system of the Azuma-Jododaira products, J.
748 Geol. Soc. Japan, 111 (2), 94-110, doi: 10.5575/geosoc.111.94 (in Japanese with English
749 abstract and figure caption)

750 Yoshida T., et al., (2014), Evolution of late Cenozoic magmatism and the crust-mantle
751 structure in the NE Japan Arc, IN: Gomez-Tuena, A., Straub, S. M., Zellmer, G. F. (eds)
752 Orogenic Andesites and Crustal Growth, Geological Society, London, Special
753 Publications, 385, 335-387, doi: 10.1144/SP385.15

754 Yoshida, Y., et al., (2012), Crustal Deformation Observed by GPS around Azuma Volcano,
755 Quart. J. Seismology, 76, 1-8 (in Japanese with English abstract and figure caption)

756 Yoshigai, Y., et al., (2019), Recent volcanic activity in Azumayama, Japan, In Abstracts
757 of AGU Fall Meeting, V51J-0227, San Francisco, CA, USA, 9-13 December 2019

758 Yoshimura, R., et al., (2018), Resistivity characterisation of Hakone volcano, Central
759 Japan, by three-dimensional magnetotelluric inversion. Earth Planets Space, 70, 66, doi:
760 10.1186/s40623-018-0848-y

761 Zhdanov, M. S., Lee, S. K., Yoshioka, K., (2006), Integral equation method for 3D
762 modeling of electromagnetic fields in complex structures with inhomogeneous

763 background conductivity, *Geophys.*, 71, G333-G345, doi: 10.1190/1.2358403

764

765 **Figure Captions**

766 **Figure 1.** Study area and the MT and GDS observation sites. (a) Location of study area.
767 (b) Regional map of study area and adjacent locations. (c) Local view of the study area
768 with the 18 MT and GDS observation sites represented by the white circles. The red
769 triangle shows the location of the active fumarole in Oana crater; black triangles designate
770 Azumayama Volcano edifices: 1. Mt. Issaikyo, 2. Azuma-kofuji, 3. Higashi-azuma, 4.
771 Naka-azuma, 5. Nishi-azuma. Contour intervals on the surface topography are labeled in
772 meters above sea level.

773 **Figure 2.** The $\tan^{-1}(\Phi_2)$ of each site at various frequencies or periods (colored circles).
774 White contour lines represent 2.5 width. The black and red triangles are the same as in
775 Figure 1.

776 **Figure 3.** RMS misfit change in terms of prior model update. Each line and character
777 show RMS misfit change depending on initial prior model (see text). Initial prior model
778 is represented by uniform subsurface resistivity.

779 **Figure 4.** Plan or map view of the final resistivity model at 0.05, 3.50, 5.50, 7.50, 9.50,
780 12.50 km depth. Background color represents the logarithmic resistivity value. Black
781 circles, white lines, red character, and black triangles, are observation sites, topographic

782 contours, Oana crater, and edifice summits, respectively (cf. Figure 1).

783 **Figure 5.** Vertical profiles of the final resistivity model in E-W direction. Top left figure
784 shows the location of each vertical profile. Background colors are the same as in Figure
785 4. The white lines are logarithmic resistivity contours. The origin of the E-W coordinate
786 is fixed at Oana crater.

787 **Figure 6.** Vertical profile of the final resistivity model in N-S direction. The origin of the
788 N-S coordinate is fixed at Oana crater. Other features are the same as those in Figures 4
789 and 5.

790 **Figure 7.** Observed (left column), calculated (center column), and misfit (right column)
791 phase tensor ellipse of each site at various periods or frequency. Observed and calculated
792 phase tensor ellipse magnitudes are normalized by observed maximum principal axis
793 magnitude at each site and period/frequency, and are filled with colors corresponding to
794 $\tan^{-1}(\Phi_2)$ designated by the color scale. The misfit phase tensor uses the definition of
795 Peacock et al. (2012), and these are filled with colors corresponding to $\Delta\Phi_{principal}$
796 (Equation 18) designated by the color scale. Azimuth of the white bars represents
797 $\alpha_{obs} + \beta_{obs} + \pi/2$ direction (length is arbitrary).

798 **Figure 8.** Plan view of CRT input and output models using checkboxes about 3 km to
799 a side. The checkboxes in the input model are embedded at 6 to 9 km depth, and those
800 in the output models are shown at 7.5 km depth (cf. Figure 10). Input checkbox
801 resistivity (red) is 1 Ωm and other blocks are 1000 Ωm except ocean (0.3333 Ωm) and air
802 blocks (10^{12} Ωm). Output models are shown at the same iteration times of the final model
803 (Figure 4) at each updated prior model. Solid lines show the calculation mesh. White
804 contour represents surface topography. NS, EW coordinates are set using Oana crater's
805 location as origin.

806 **Figure 9.** Same with Figure 8, but using checkboxes about 5 km to a side. The
807 checkboxes are embedded at 5 to 10 km depth, and the output models are shown at 7.5
808 km depth (cf. Figure 10).

809 **Figure 10.** Vertical profile in E-W direction of CRT input and output models. Left and
810 right columns represent the models using checkboxes with one side 3 and 5 km,
811 respectively.

812 **Figure 11.** Perspective view of isosurface of (a) 3 and (b) 1 Ωm in 3 to 15 km. Bottom of
813 each figure shows observation site (solid circle) edifice (solid triangle) surface

814 topography (black contour line), and the vertical projection of the isosurface (shade).

815 **Figure 12.** F-statistic change of each site in terms of resistivity change of target area
816 shown in Figure 11. (a) F-statistic change obtained by changing resistivity inside
817 isosurface in Figure 11a. (b) Same with (a), but obtained by changing resistivity inside
818 Figure 11b. Confidence level of 95, 90, and 67 % are shown in blue, red, and green lines,
819 respectively. The 67 % and 90 % CIR in (a) are determined to be 0.3 to 5 Ωm (dark shade)
820 and 0.02 to 70 Ωm (light shade), respectively. The 95 % CIR in (a) and 67 to 95 % CIR
821 in (b) are not available.

822 **Figure 13.** Mogi source locations of the two (solid circle) or three (solid star) inflation
823 source models by Seki et al. (2020) superimposed on the N-S vertical profile of the final
824 resistivity model (H' - H profile in Figure 6).

825 **Figure 14.** Bulk resistivity (solid line) of dacitic melt and rock complex at 900 °C, 0.15
826 GPa as a function of melt fraction and of water content in the dacitic melt. Gray shaded
827 area represents the 67 % CIR of Figure 11a, and the solid lines show water content of
828 dacitic melt in weight percent. Note that the upper and lower bound of 67 % CIR is bottom
829 and top of the gray shaded area, respectively. Melt resistivity is calculated from

830 Laumonier et al. (2015). Solid phase resistivity is fixed at 1000 Ωm (e.g. granite data of
831 Kariya & Shankland, 1983).

832 **Figure 15.** Bulk resistivity (solid line) of andesitic melt and rock complex at 900 °C, 0.29
833 GPa as a function of melt fraction and of water content in the andesitic melt. Melt
834 resistivity calculations from Guo et al. (2017) are shown by the broken line, and from
835 Laumonier et al. (2017) are shown by the solid line. Solid phase resistivity is fixed at 500
836 Ωm (e.g. rhyolite data of Kariya & Shankland, 1983). Others are the same as Figure 14.

837 **Figure 16.** Bulk resistivity of two phases (hydrothermal fluid-rock) as a function of the
838 hydrothermal fluid fraction (solid line). Hydrothermal fluid resistivity is assumed to be
839 0.1 or 0.3 Ωm . Rock resistivity is fixed at 1000 Ωm (cf. Figure 14). Green, orange, and
840 pink columns show percolation threshold porosity in effusive and explosive eruptions,
841 and change point of permeability-porosity relationship, respectively. Red and green lines
842 show the upper bounds of 67 % and 90 % CIR of the conductor (cf. Figure 11a). Oblique
843 pattern represents likely resistivity range at the Mogi inflation source location, assuming
844 that the upper bound of CIR of the conductor restricts the lower bound of resistivity at
845 the Mogi inflation source.

Figures

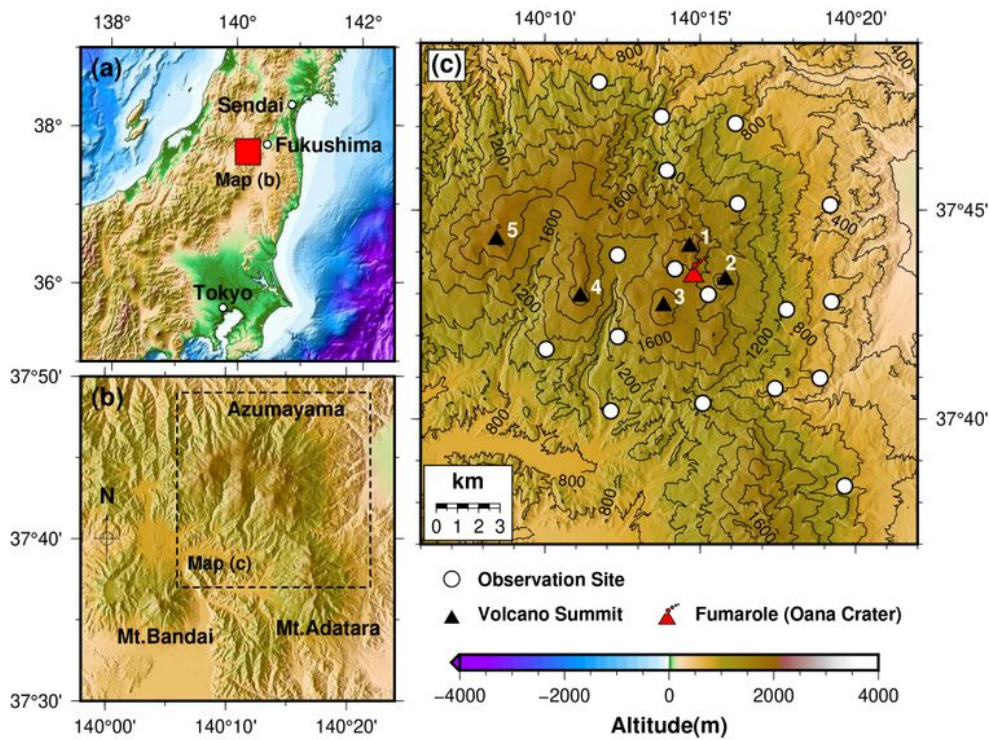


Figure 1

Study area and the MT and GDS observation sites. (a) Location of study area. (b) Regional map of study area and adjacent locations. (c) Local view of the study area with the 18 MT and GDS observation sites represented by the white circles. The red triangle shows the location of the active fumarole in Oana crater;

black triangles designate Azumayama Volcano edifices: 1. Mt. Issaikyo, 2. Azuma-kofuji, 3. Higashi-azuma, 4. Naka-azuma, 5. Nishi-azuma. Contour intervals on the surface topography are labeled in meters above sea level. Note: The designations employed and the presentation of the material on this map do not imply the expression of any opinion whatsoever on the part of Research Square concerning the legal status of any country, territory, city or area or of its authorities, or concerning the delimitation of its frontiers or boundaries. This map has been provided by the authors.

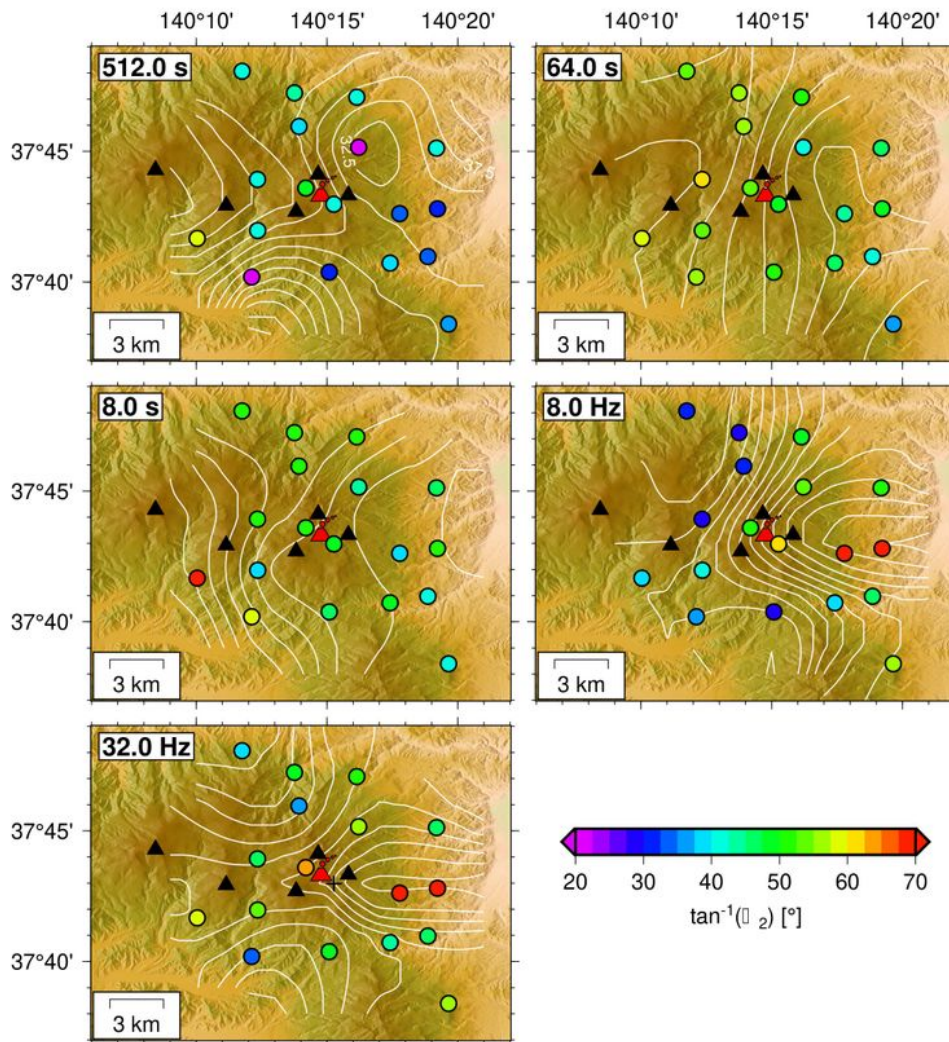


Figure 2

The $\tan^{-1}(\Phi_2)$ of each site at various frequencies or periods (colored circles). White contour lines represent 2.5 width. The black and red triangles are the same as in Figure 1.

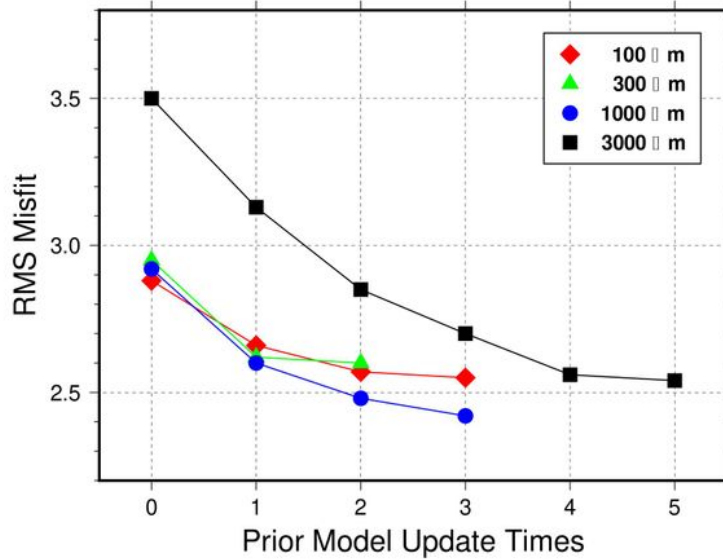


Figure 3

RMS misfit change in terms of prior model update. Each line and character show RMS misfit change depending on initial prior model (see text). Initial prior model is represented by uniform subsurface resistivity.

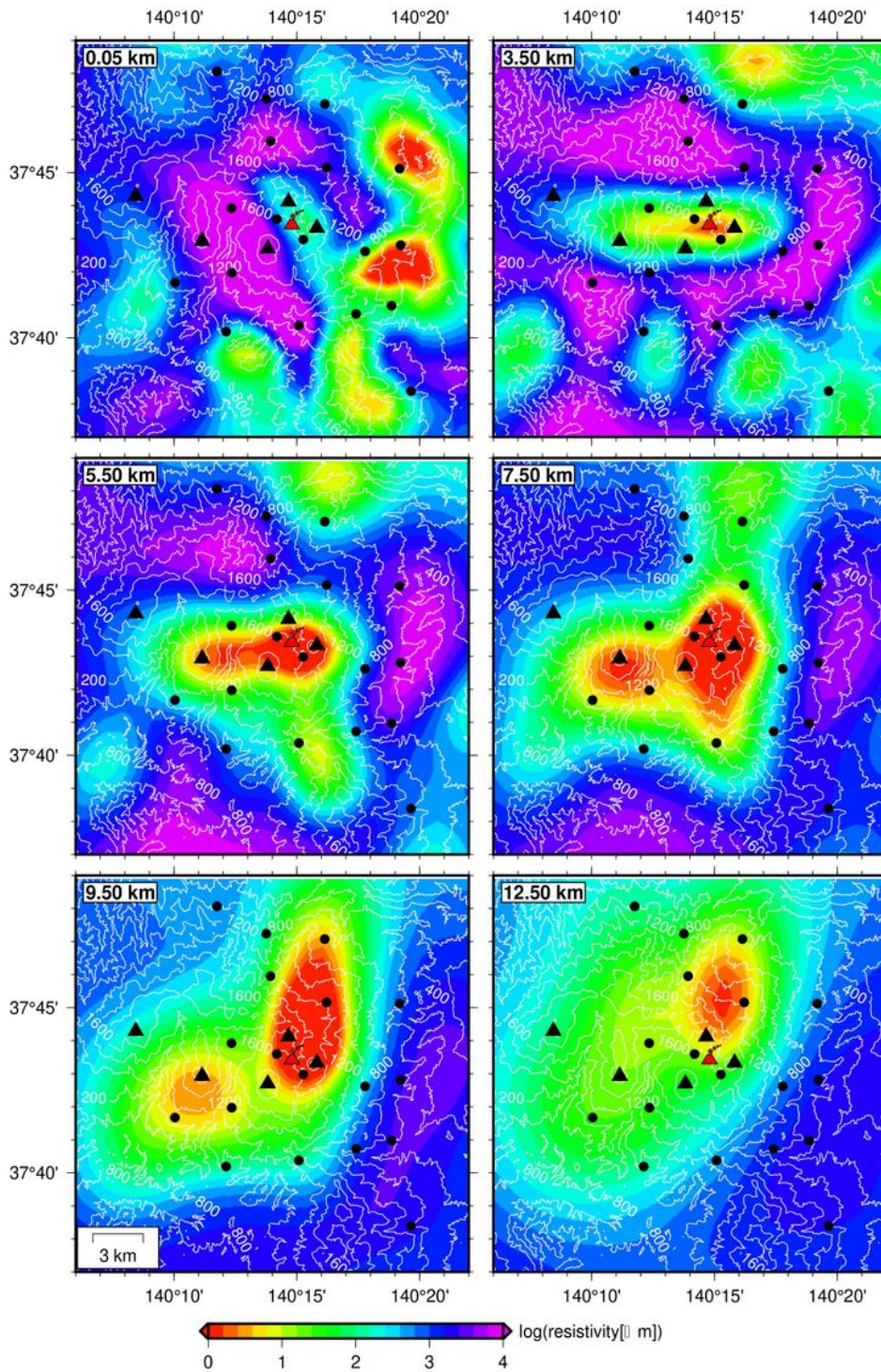


Figure 4

Plan or map view of the final resistivity model at 0.05, 3.50, 5.50, 7.50, 9.50, 12.50 km depth. Background color represents the logarithmic resistivity value. Black circles, white lines, red character, and black triangles, are observation sites, topographic contours, Oana crater, and edifice summits, respectively (cf. Figure 1).

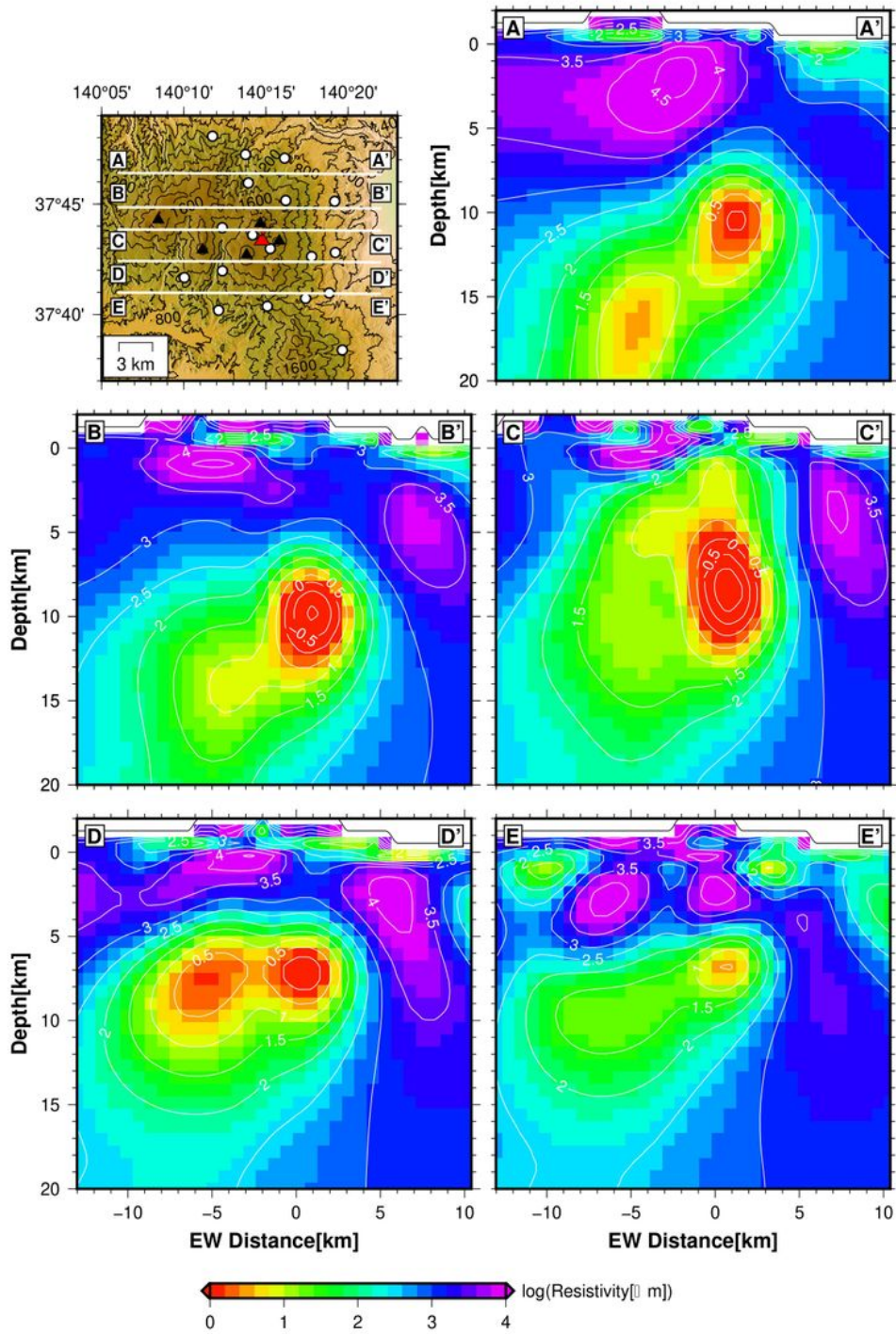


Figure 5

Vertical profiles of the final resistivity model in E-W direction. Top left figure shows the location of each vertical profile. Background colors are the same as in Figure 4. The white lines are logarithmic resistivity contours. The origin of the E-W coordinate is fixed at Oana crater.

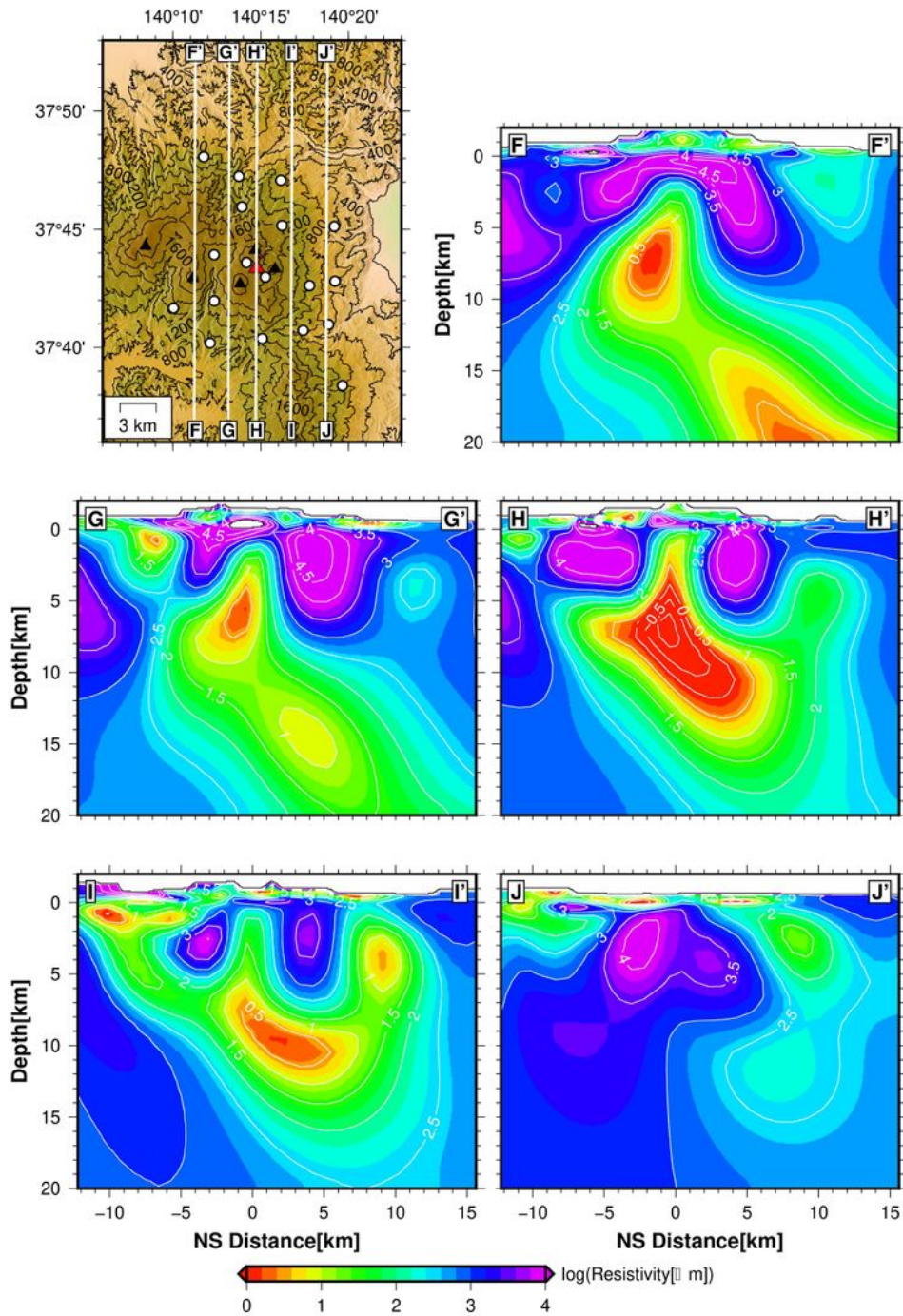


Figure 6

Vertical profile of the final resistivity model in N-S direction. The origin of the N-S coordinate is fixed at Oana crater. Other features are the same as those in Figures 4 and 5.

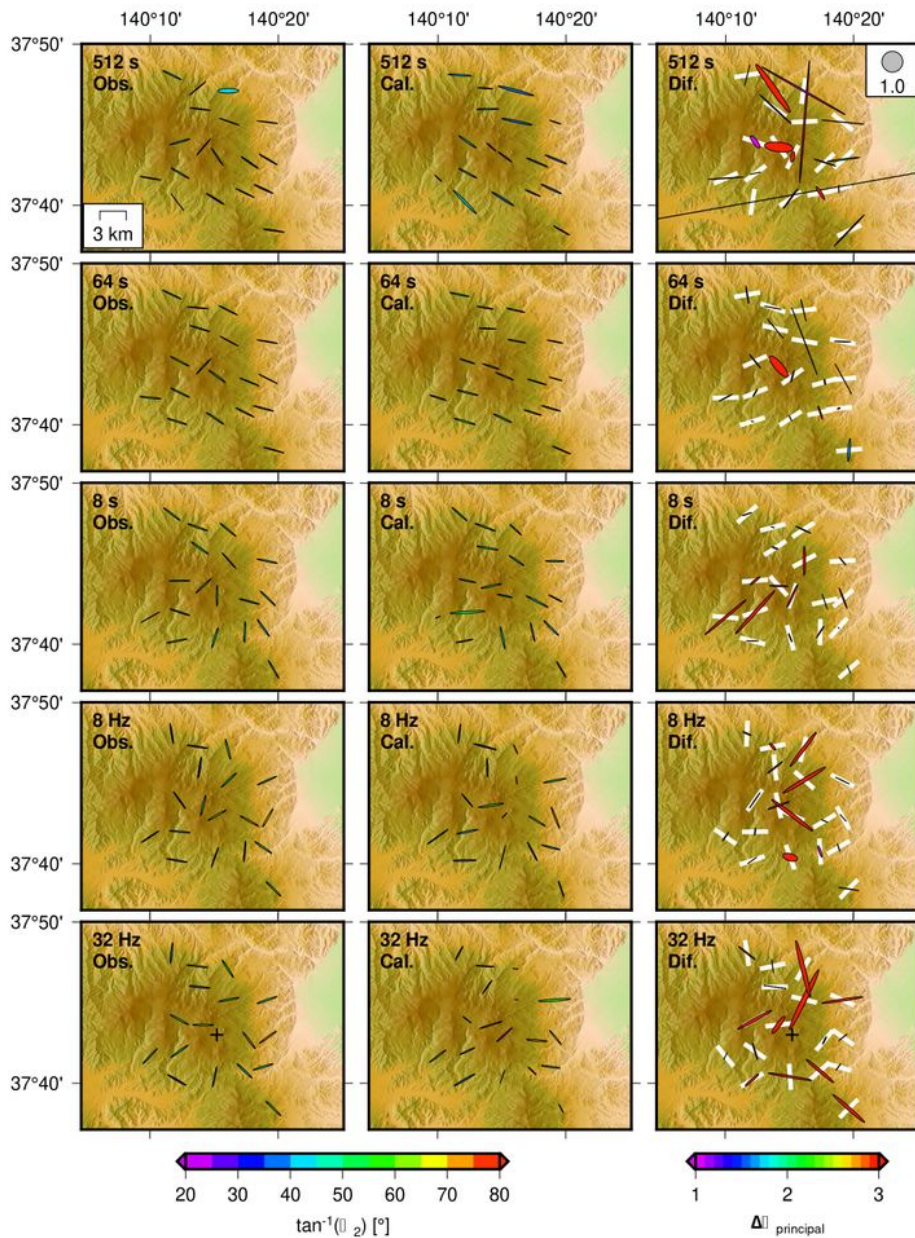


Figure 7

Observed (left column), calculated (center column), and misfit (right column) phase tensor ellipse of each site at various periods or frequency. Observed and calculated phase tensor ellipse magnitudes are normalized by observed maximum principal axis magnitude at each site and period/frequency, and are filled with colors corresponding to $\tan^{-1}(\Phi_2)$ designated by the color scale. The misfit phase tensor uses the definition of Peacock et al. (2012), and these are filled with colors corresponding to $\Delta\Phi_{\text{principal}}$

(Equation 18) designated by the color scale. Azimuth of the white bars represents $\alpha_{obs} + \beta_{obs} + \pi/2$ direction (length is arbitrary).

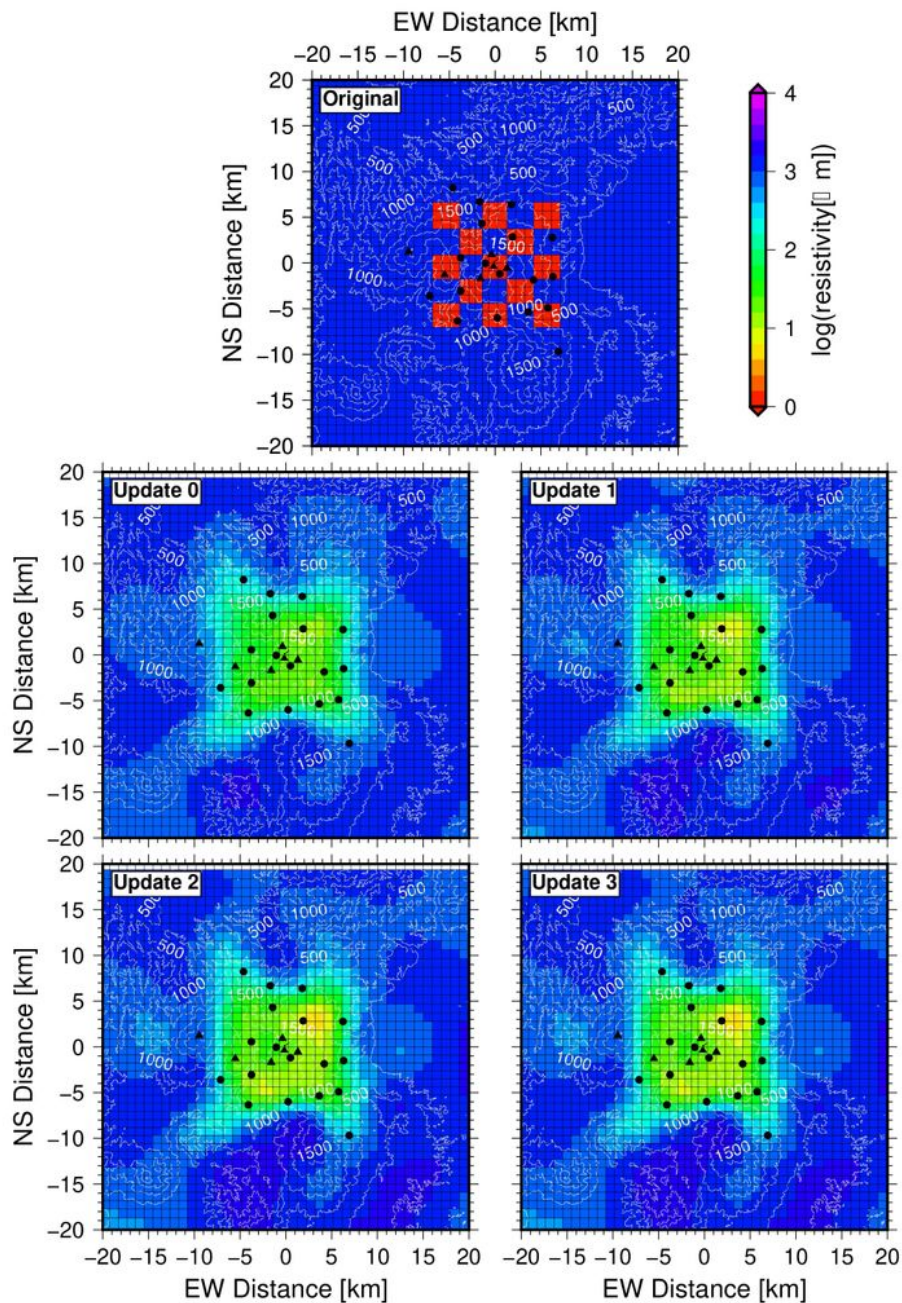


Figure 8

Plan view of CRT input and output models using checkerboxes about 3 km to a side. The checkerboxes in the input model are embedded at 6 to 9 km depth, and those in the output models are shown at 7.5 km depth (cf. Figure 10). Input checkbox resistivity (red) is 1 Ωm and other blocks are 1000 Ωm except

ocean ($0.3333 \Omega\text{m}$) and air blocks ($1012 \Omega\text{m}$). Output models are shown at the same iteration times of the final model (Figure 4) at each updated prior model. Solid lines show the calculation mesh. White contour represents surface topography. NS, EW coordinates are set using Oana crater's location as origin.

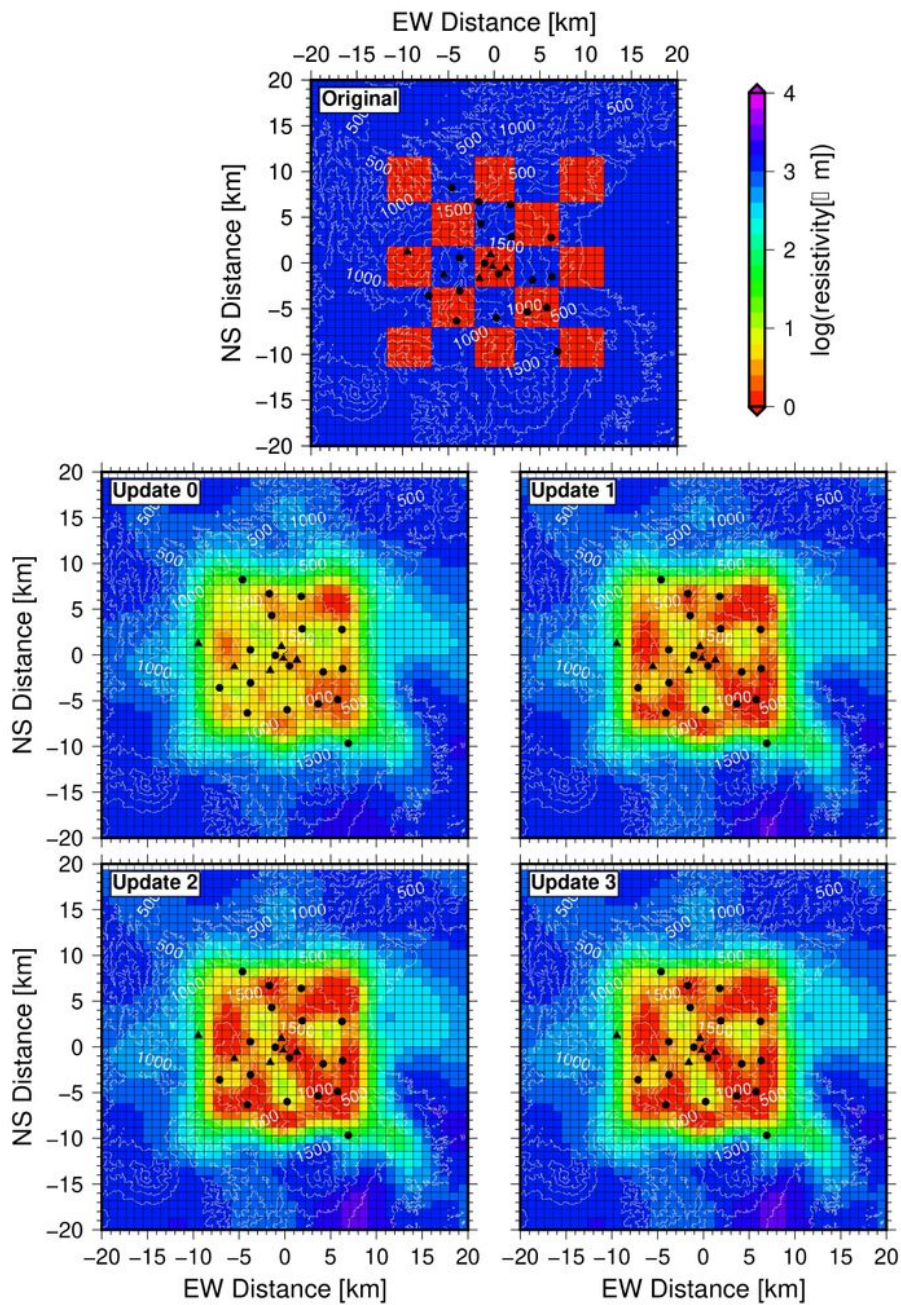


Figure 9

Same with Figure 8, but using checkboxes about 5 km to a side. The checkboxes are embedded at 5 to 10 km depth, and the output models are shown at 7.5 km depth (cf. Figure 10).

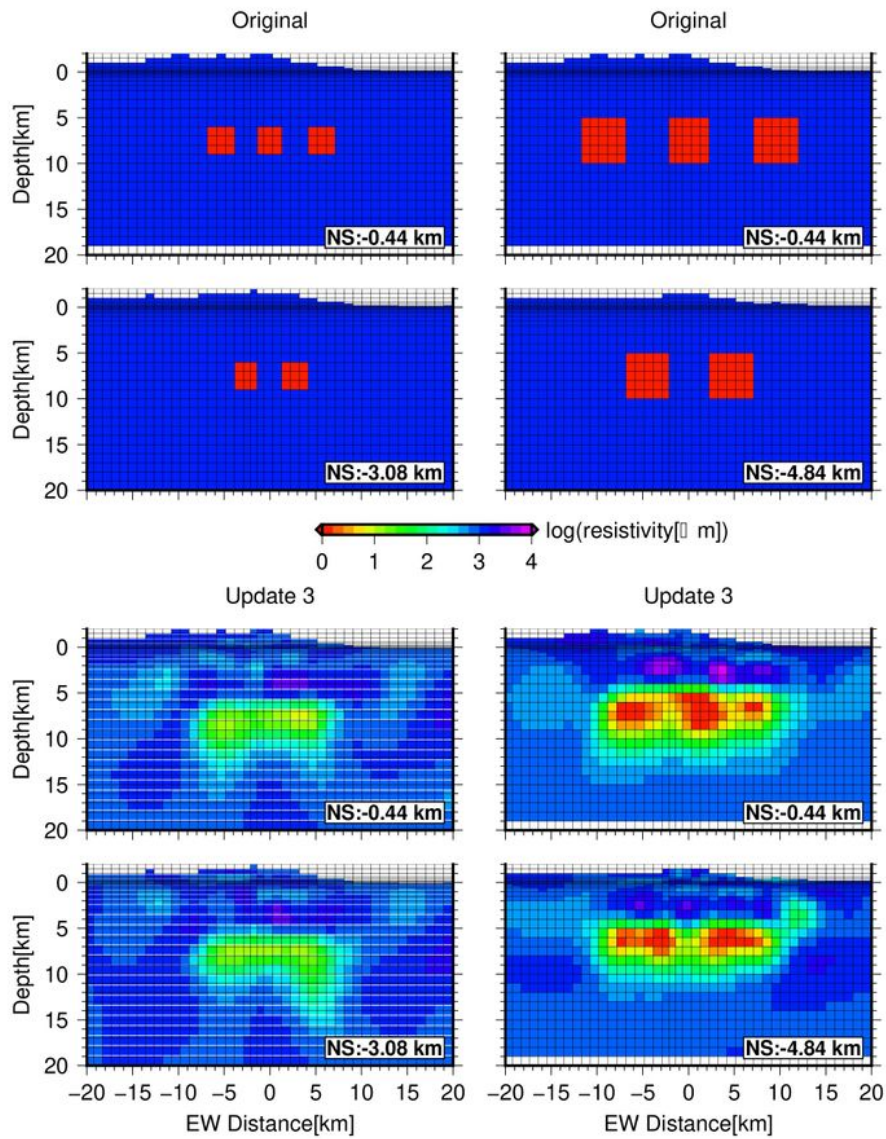


Figure 10

Vertical profile in E-W direction of CRT input and output models. Left and right columns represent the models using checkboxes with one side 3 and 5 km, respectively.

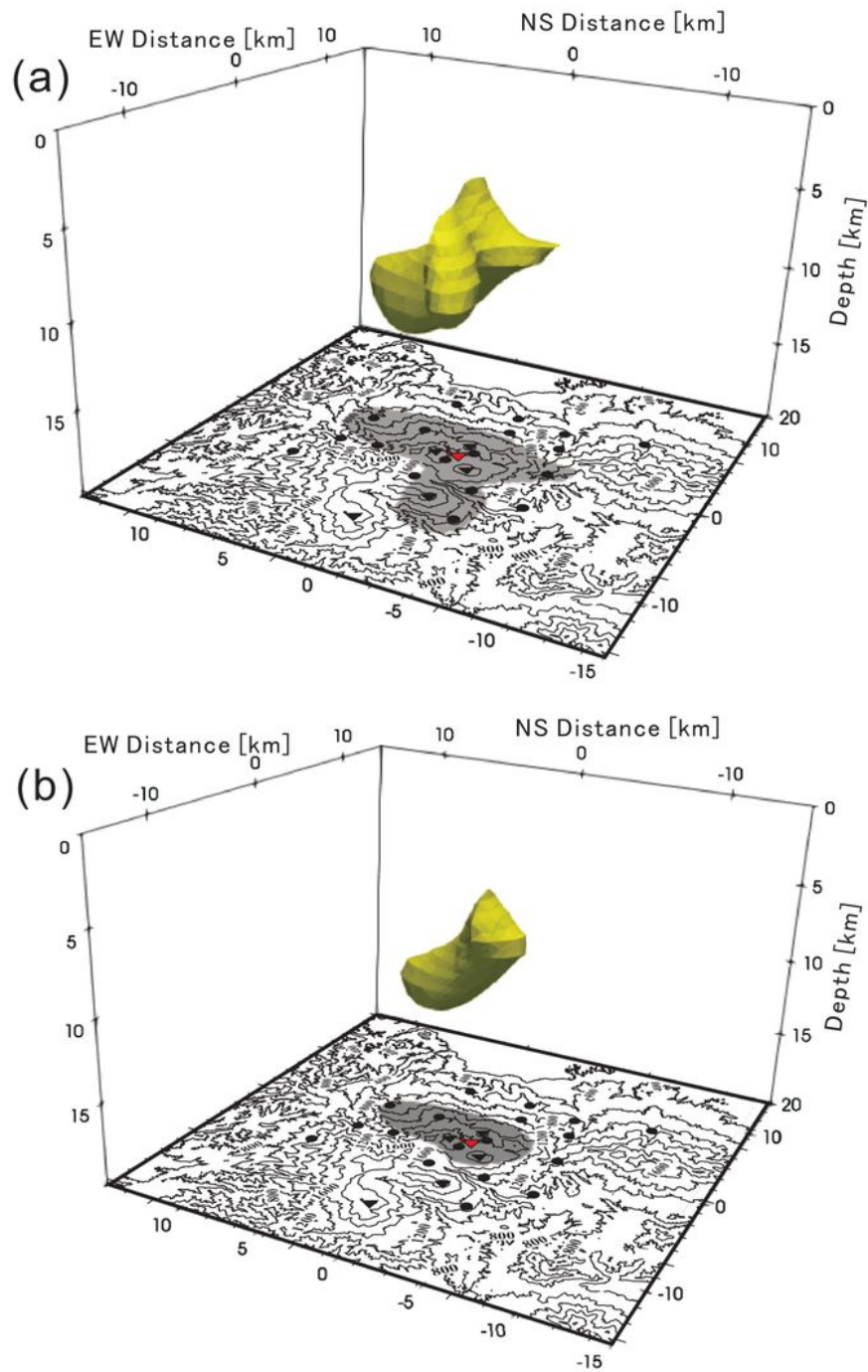


Figure 11

Perspective view of isosurface of (a) 3 and (b) 1 Ωm in 3 to 15 km. Bottom of each figure shows observation site (solid circle) edifice (solid triangle) surface topography (black contour line), and the vertical projection of the isosurface (shade).

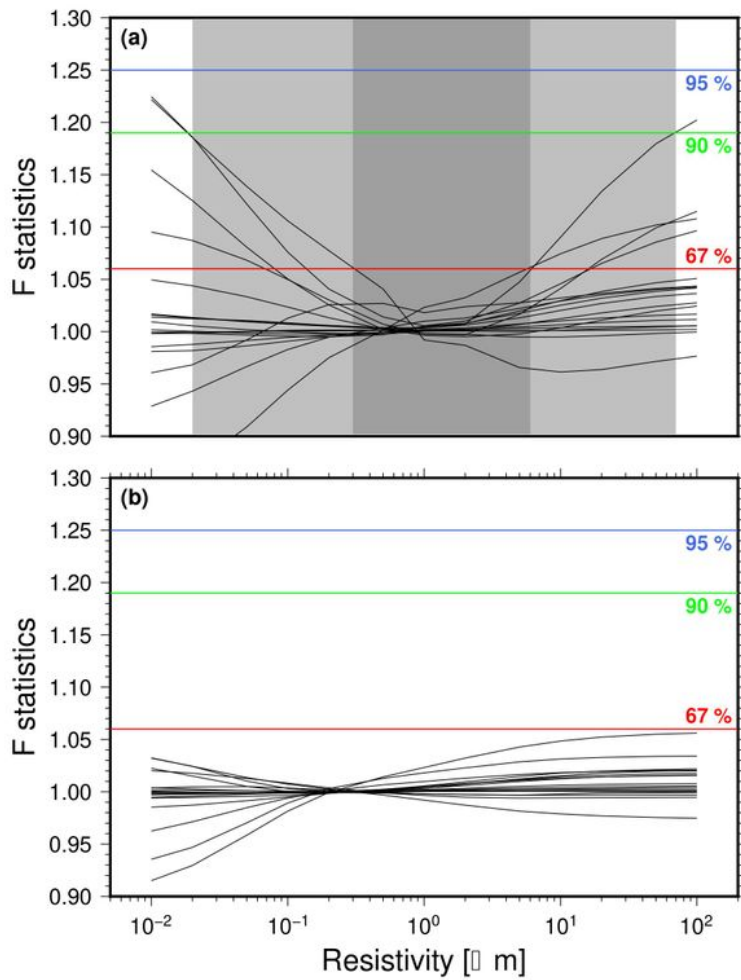


Figure 12

F-statistic change of each site in terms of resistivity change of target area shown in Figure 11. (a) F-statistic change obtained by changing resistivity inside isosurface in Figure 11a. (b) Same with (a), but obtained by changing resistivity inside Figure 11b. Confidence level of 95, 90, and 67 % are shown in blue, red, and green lines, respectively. The 67 % and 90 % CIR in (a) are determined to be 0.3 to 5 Ωm (dark

shade) and 0.02 to 70 Ωm (light shade), respectively. The 95 % CIR in (a) and 67 to 95 % CIR in (b) are not available.

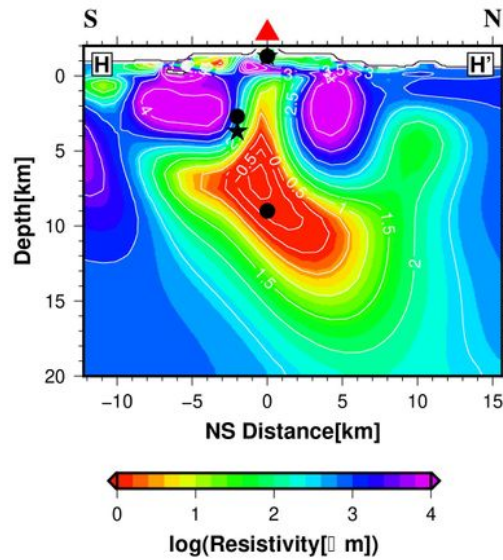


Figure 13

Mogi source locations of the two (solid circle) or three (solid star) inflation source models by Seki et al. (2020) superimposed on the N-S vertical profile of the final resistivity model (H'-H profile in Figure 6).

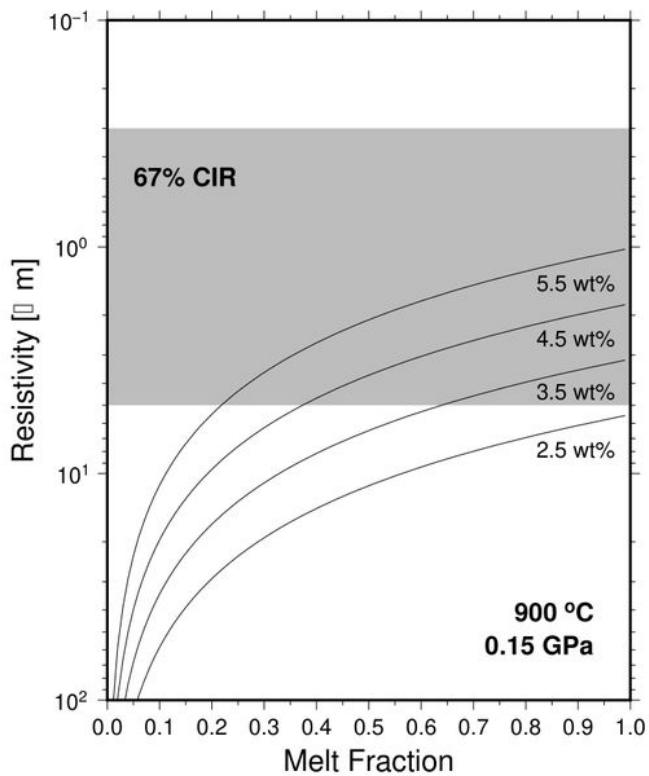


Figure 14

Bulk resistivity (solid line) of dacitic melt and rock complex at 900 °C, 0.15 GPa as a function of melt fraction and of water content in the dacitic melt. Gray shaded area represents the 67 % CIR of Figure 11a, and the solid lines show water content of dacitic melt in weight percent. Note that the upper and lower bound of 67 % CIR is bottom and top of the gray shaded area, respectively. Melt resistivity is calculated

from Laumonier et al. (2015). Solid phase resistivity is fixed at 1000 Ωm (e.g. granite data of Kariya & Shankland, 1983).

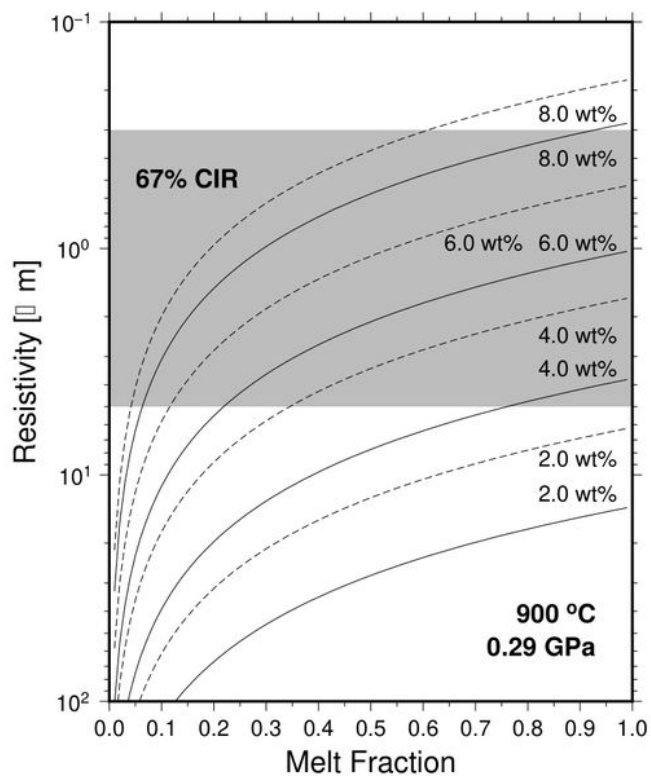


Figure 15

Bulk resistivity (solid line) of andesitic melt and rock complex at 900 °C, 0.29 GPa as a function of melt fraction and of water content in the andesitic melt. Melt resistivity calculations from Guo et al. (2017) are shown by the broken line, and from Laumonier et al. (2017) are shown by the solid line. Solid phase

resistivity is fixed at 500 Ωm (e.g. rhyolite data of Kariya & Shankland, 1983). Others are the same as Figure 14.

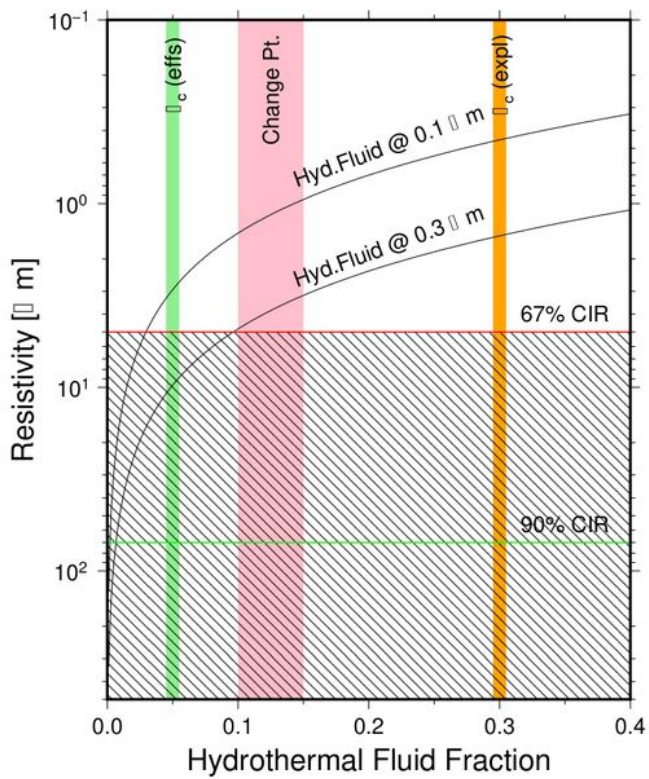


Figure 16

Bulk resistivity of two phases (hydrothermal fluid-rock) as a function of the hydrothermal fluid fraction (solid line). Hydrothermal fluid resistivity is assumed to be 0.1 or 0.3 Ωm . Rock resistivity is fixed at 1000 Ωm (cf. Figure 14). Green, orange, and pink columns show percolation threshold porosity in effusive and

explosive eruptions, and change point of permeability-porosity relationship, respectively. Red and green lines show the upper bounds of 67 % and 90 % CIR of the conductor (cf. Figure 11a). Oblique pattern represents likely resistivity range at the Mogi inflation source location, assuming that the upper bound of CIR of the conductor restricts the lower bound of resistivity at the Mogi inflation source.

Supplementary Files

This is a list of supplementary files associated with this preprint. Click to download.

- [GraphicalAbstract.png](#)
- [SupplementalMaterial1.pdf](#)
- [SupplementalMaterial2.pdf](#)